

AMERICAN UNIVERSITY OF BEIRUT

CELL-SPECIFIC ION-CHANNEL KINETICS IMPROVE  
NEURONAL MODEL FITTING ACROSS CHAOTIC  
DYNAMICAL REGIMES

by  
ZEINA KHODOR NOUREDDINE

A thesis  
submitted in partial fulfillment of the requirements  
for the degree of Master of Science in Biomedical Engineering  
to the Biomedical Engineering Program  
of the Maroun Semaan Faculty of Engineering and Architecture  
and Faculty of Medicine  
at the American University of Beirut

Beirut, Lebanon  
January 2026

AMERICAN UNIVERSITY OF BEIRUT

CELL-SPECIFIC ION-CHANNEL KINETICS IMPROVE  
NEURONAL MODEL FITTING ACROSS CHAOTIC  
DYNAMICAL REGIMES

by

ZEINA KHODOR NOUREDDINE

Approved by:

---

Dr. Arij Daou, Assistant Professor  
Biomedical Engineering Program

Advisor

---

Dr. Wassim Nasreddine, Associate Professor  
Department of Neurology

Co-Advisor

---

Dr. Jason Amatory, Associate Professor  
Biomedical Engineering Program

Member of Committee

---

Dr. Naseem Daher, Associate Professor  
Department of Electrical and Computer Engineering  
Department of Mechanical Engineering

Member of Committee

Date of thesis defense: January 30, 2026

## ACKNOWLEDGEMENT

I sincerely thank my advisor, Dr. Arij Daou, for his guidance and support throughout this work.

I am deeply grateful to my parents for their unconditional love and support.

I would like to thank my husband for his constant support, endless patience and encouragement. I am also thankful to my children for being my greatest source of motivation and joy.

Special thanks to Mrs. Nina Ghannam, Senior Library Specialist in Jafet Library, for her kind assistance with the library submission process.

Finally, I thank all my friends and colleagues who supported me with kind words, support, and shared moments of laughter during stressful times.

# ABSTRACT

## OF THE THESIS OF

Zeina Khodor Nouredine

for Master of Science in Biomedical Engineering  
Major: Biomedical Engineering

Title: Cell-specific Ion-Channel Kinetics Improve Neuronal Model Fitting Across Chaotic Dynamical Regimes

Modeling neuronal activity is central to understanding brain dynamics, yet fitting biophysically realistic neuron models to electrophysiological data remains difficult because neuronal membranes are highly nonlinear and their responses depend strongly on the dynamical regime explored. A major practical barrier is that standard fitting strategies often rely on fixed (“one-size-fits-all”) parameter sets and error functions that inadequately reflect spike waveform structure, leading to fits that appear good under one protocol but fail to generalize under other protocols. Here we show that pseudo-noisy (chaotic) stimuli expose regime-dependent limits of fixed-parameter neuron models, and that robust performance requires cell-specific kinetic fitting coupled to feature-based evaluation. We designed a library of pseudo-noisy current stimuli that vary in amplitude distributions, temporal structure, and frequency content, and applied them during whole-cell patch clamp recordings from premotor cortex neurons in zebra finches. We then drove a biophysically realistic conductance-based model, with ionic currents guided by pharmacological identification, using the same stimuli. Using a nonlinear data-assimilation framework, we estimated unobserved state variables and unknown parameters from responses to one chaotic stimulus and tested generalization by predicting responses to other chaotic stimuli. We found that a model fitted under a single chaotic input often reproduces neuronal behavior only within the dynamical regime explored by that stimulus; when a different chaotic stimulus drives the neuron through new voltage ranges and gating-variable states, fixed-parameter fits frequently break down, revealing mismatches in underlying ion-channel dynamics. In contrast, treating each neuron individually and fitting its activation/inactivation kinetics yields markedly improved fits and more reliable cross stimulus predictions. To quantify these effects, we introduced a feature-based error function tailored to chaotic stimulation, capturing spike timing and waveform heuristics (e.g., threshold, amplitude, width/time-to-peak, after-hyperpolarization, and subthreshold structure). Together, our results provide a principled framework - chaotic stimulus design, cell-specific kinetic identification, and feature-based error trade-off analysis, for evaluating when neuron models accurately capture ion-channel dynamics and when apparent fits are regime-restricted.

## TABLE OF CONTENTS

ACKNOWLEDGEMENT.....	3
ABSTRACT .....	1
ILLUSTRATIONS.....	4
TABLES .....	6
EQUATIONS .....	7
INTRODUCTION.....	10
LITERATURE REVIEW .....	13
A. Complexity and Nonlinearity of Physiological Systems.....	13
B. Criteria for the Evaluation of Proposed Models.....	19
1. Victor and Purpura Method .....	20
2. Van Rossum Method .....	21
3. Schreiber et al. Similarity Measure.....	21
4. Bivariate SPIKE-distance .....	24
C. Hodgkin Huxley Model .....	28
D. Data Assimilation .....	30
RESEARCH GAP .....	36
METHODOLOGY .....	38
A. Hodgkin Huxley Model Fitting .....	39

B. Defining the Ionic Channels .....	39
1. Leak Current .....	39
2. Sodium Ionic Channels .....	40
3. Potassium Ionic Channel <b><i>IK</i></b> .....	41
4. Persistent <b><i>Na</i></b> +Current .....	41
5. A – type <b><i>K</i></b> + Current <b><i>IA</i></b> .....	42
6. High Threshold L- Type <b><i>Ca2</i></b> + Current.....	42
7. Low Threshold T-type <b><i>Ca2</i></b> +Current.....	43
8. Small Conductance <b><i>Ca2</i></b> + Activated <b><i>K</i></b> + Current <b><i>ISK</i></b> .....	44
9. Hyperpolarization- Activated Cation Current <b><i>Ih</i></b> .....	45
10. Channel Gating Dynamics .....	46
C. Model Input.....	52
D. Model Assessment .....	54
1. Features Extraction .....	54
2. Comparing spikes .....	55
3. Parameter variations .....	57
4. Utilizing a New Error Metric.....	57
5. Spike Timing.....	58
6. Error in Voltage Threshold:.....	58
7. Error in spikes' width .....	59
8. Error in Time to Peak.....	59
9. Using HPC cluster .....	59
RESULTS .....	61
DISCUSSION.....	81
CONCLUSION .....	88
REFEREENCES.....	89

# ILLUSTRATIONS

## Figure

1. Manual and Automated Fits for Model and Biological Trace .....	19
2. Victor-Purpura Spike Train Distance. ....	21
3. Van Rossum Distance and Schreiber Methods.....	23
4. The Bivariate Spike-Distance .....	26
5. Hodgkin–Huxley Model of Biological Neurons.....	30
6. Data Assimilation Method.....	32
7. Data Assimilation Applied to the Noisy Data (Voltage and Injected current). ..	34
8. Workflow of the Methodology. ....	38
9. Different Waveforms of the Applied Pseudo-Noisy Current Presented to the Hvcx Model. ....	53
10. The Injected Stimulating Current $I(t)$ Presented to the HVC <sub>x</sub> Model.....	54
11. The Main Features Extracted from The Trace.....	55
12. Overlay of Biological (Blue) And Hodgkin–Huxley Model-Simulated (Red) Voltage.....	57
13. Biological and Model Trace Comparison. ....	61
14. Comparison Between the Biological Spike (Blue) and the Classical Hodgkin–Huxley Model Spike (Black). ....	62
15. Comparison Between Biological Voltage Traces and Model Simulations.....	64
16. Brute Force Search Results for Optimal Parameters for Each Neuron.....	65
17. Model Closely Matches Biological Spike Timing and Shape .....	67
18. Sample of Three Biological Recordings.....	68
19. Model and Biological Spike Trains Aligned Across Epochs .....	69
20. Feature–Feature Trade-Off Plots .....	71
21. Spike Overlays and Feature-Error Trade-Offs Across Parameters.....	75
22. Averaged Feature-Specific Errors as a Function of Sodium Conductance .....	76
23. Averaged Feature-Specific Errors as a Function of Potassium Conductance. ...	77

24. Boxplots Showing the Distribution of Optimized Model Parameters across Neurons.....	78
25. Boxplots Showing the Distribution of Optimized Model Parameters across Neurons.....	79
26. A Final Optimized Plot Showing the Model and Biological Traces Overlaid. ..	80

## TABLES

Table

1. Constant Parameter Values Used in All Simulations. ....	46
--	----

# EQUATIONS

## Equation

1. Van Rossum method .....	21
2. Time of Preceding Spike.....	24
3. Time of the Following Spike .....	24
4. Instantaneous Interspike Interval .....	24
5. Local Weighted Average .....	25
6. Instantaneous Absolute Difference .....	25
7. Normalized Timescale Invariance .....	25
8. Weighted Average .....	25
9. Similarity Profile.....	25
10. Bivariate SPIKE-Distance .....	26
11. Root Mean Square Error .....	27
12. Current Balance Equations .....	29
13. Differential Equation Describing the Model .....	31
14. Membrane Voltage Equation (Current Balance Equation).....	39
15. Leak Current .....	39
16. Sodium Current.....	40
17. Potassium Current.....	41
18. Persistent Sodium Current .....	41
19. Boltzmann Steady-State Activation of $I_{Nap}$ .....	41
20. Steady- State Inactivation Function for Sodium Channels.....	41
21. Voltage-Dependant Sodium Inactivation Rate( Forward rate).....	42
22. Voltage-Dependant Sodium Inactivation Rate (Backward Rate).....	42
23. A – type $K^{+}$ Current .....	42
24. Boltzmann Activation of $I_A$ .....	42
25. First - Order Inactivation Dynamics of the A-type Potassium Current .....	42
26. High Threshold L- Type $Ca^{2+}$ Current.....	42

27. Steady-State Activation Function of the L-type Calcium Current .....	43
28. Low Threshold L- type $\text{Ca}^{2+}$ Current.....	43
29. Steady-State Activation Function of the T-type Calcium Current .....	43
30. Inactivation Function of the T-type Calcium Current .....	43
31. Slowly Recovery Dynamics of T-type Calcium Current.....	44
32. Steady-State Recovery Function of the T-type Calcium Current .....	44
33. Small Conductance $\text{Ca}^{2+}$ Activated $\text{K}^+$ Current.....	44
34. Steady-State Activation Function of the SK Current .....	44
35. Dissociation Constant of the $\text{Ca}^{2+}$ .....	44
36. Hyperpolarization- Activated Cation Current.....	45
37. Fast Activation Components.....	45
38. Time Constant.....	45
39. Slow Activation Component.....	45
40. Fast Sodium Channel Activation Gating Equation.....	47
41. Voltage-Dependent Sodium Activation Rate Constant. ....	48
42. Voltage-Dependent Sodium Deactivation Rate Constant.....	48
43. Fast Sodium Channel Inactivation Gating Equation.....	48
44. Steady-State Inactivation Function of the Sodium Channel .....	48
45. Voltage-Dependent Sodium Inactivation Rate Constant .....	48
46. Voltage-Dependent Sodium Recovery Rate Constant.....	48
47. Voltage-Dependent Potassium Activation Rate Constant .....	50
48. Voltage-Dependent Potassium Deactivation Rate Constant.....	50
49. Absolute Difference of Spike Time for Model and Biological Trace .....	58
50. Averaged Spike Time Error.....	58
51. Averaged Threshold Error .....	58
52. Half Amplitude .....	59
53. Spike Width .....	59
54. Averaged Spike Width Error .....	59

55. Time to Peak .....	59
56. Averaged Time to Peak Error .....	59

# CHAPTER I

## INTRODUCTION

The brain is a complex system that exhibits different intricate connections among its various components. These connections underlie the brain's ability to perform its complex functions allowing it to process information, perceive the environment, and generate different behaviors and responses. Understanding these complex connections at the level of neuronal responses is a fundamental goal in computational neuroscience.

Therefore, electrophysiologists centered on replicating the human brain by developing computational models to simulate the brain's activity. These models are designed to meticulously replicate the neuron's morphological and electrical behavior in response to a given stimulus. Computational neuronal models are essential in paving the way in understanding the different nonlinear functions of the brain. Computational models can provide key insights into the relation between some neuronal properties and observed behaviors or pathological conditions. They also play a vital role in accelerating clinical research by allowing simulations that mimic the brain's nonlinear behavior. Among these models is the Hodgkin Huxley model, which is a fundamental biophysical model in Neuroscience that established a crucial link between components at the membrane level of the ionic channels and the boarder scale of the signal transmission within neuronal networks. Action potentials originating from the neurons exhibit distinct electrophysiological characteristics crucial for elucidating ion channel kinetics and neuronal firing dynamics. These features, such as amplitude, duration, frequency, spikes timing, threshold timings, threshold voltage, and subthreshold oscillations are essential in understanding the underlying mechanisms governing neuronal excitability and

information processing within the nervous system. Although fits originating from computational modeling have a significant role in analyzing different dynamical systems, the growing complexity of neurons and their nonlinearity in the brain presents a significant challenge: finding a decent model fit and optimal parameters that truly resemble the neuronal output. There is never a 100% accurate model that fits biological data given the high nonlinearity in biological systems. Central to this challenge is the absence of an error function that can assess the goodness of a fit.

The aim of our study is to optimize neuronal models fits by utilizing several key elements that play a vital role in elucidating the complex behavior of neurons and provide better fitted models, this is done by: developing the appropriate stimuli, estimating the correct parameters to fit the model through inspection of Hodking Huxley Model, and developing a feature error analysis capable of assessing the model fits. Traditionally, electrophysiologists inject neurons with step or ramp currents to elicit responses in the neurons, and they judge the neuron's dynamics based on these responses. However, the activation and inactivation kinetics of neurons are not fully unveiled via step currents. Hence, we hypothesize the use of a complex chaotic stimuli that can be better at unfolding the intricate dynamics of neurons. This current consists of a pseudo noisy waveform that fluctuates between negative and positive values. By using this current we aim at visiting the different complex states that can occur during signal transmission which may not be resembled in step currents stimulated neurons.

The developed chaotic stimuli are being injected to cortical neurons of the zebra finch. We will use the data to impose the data assimilation technique from physical sciences which will allow us to estimate the targeted model parameters. The assimilated model will then be used to forecast the whole model trace to check the model's accuracy.

We hypothesize that by using data assimilation we can accurately estimate and predict the whole state of the model. This procedure advances previous fitting methods as it enables the determination of temporal evolution of multiple unobserved variables. Additionally, it can precisely determine the values of many parameters that are part of the dynamical equations including those that contribute nonlinearly to the neuronal model. This capability represents a significant improvement in the field of parameter and state estimation.

We then optimize model fits by analyzing the tradeoffs between the different error metrics between the model and biological traces, given the pseudo-noisy stimuli. To test our model, we will use a biophysically realistic model which is based on ion channels that had been identified pharmacologically. This model will replicate the different spiking behavior when altering the conductance's of specific ionic channels. We then simulate this model by a chaotic stimulus, the fits are incorporated into the assimilation procedure to find the best model fits. These fits will be assessed using the proposed error function.

## CHAPTER II

### LITERATURE REVIEW

This chapter provides an overview about the complexity in the nervous system and the challenges encountered when modeling any mechanism of the brain. We first delve into the complexities and non-linearities in the brain due to the different interactions present within the neural network. We then describe the challenges encountered with the computational modeling of the nonlinear response of neurons. We also discuss the absence of a well-defined error function for evaluating the goodness of a fit and mention other methods from literature used to assess the goodness of a fit. We highlight on the importance of the error function that considers the different features of an action potential. In the sections that follow we explore the data assimilation method as mathematical technique to find the best model fit. We then present the Hodgkin Huxley model, a foundational model in computational neuroscience that describes that is used for fitting our model.

#### **A. Complexity and Nonlinearity of Physiological Systems**

The biological system, in particular the brain, demonstrates a remarkable level of complexity, due to the presence of intricate molecular interactions within the cells to the dynamic network of the brain. Neurons constitute the building blocks of the brain and central nervous system. They exhibit nonlinear firing patterns, which implies that their firing rates may differ even when they are interconnected [Li et al. \(2024\)](#). Neurons communicate with each other via action potentials or spikes. In response to any stimuli, the neurons in the brain fire action potentials that exhibit different electrophysiological

properties crucial for understanding the brain activity. At the level of a single neuron, spikes serve as the primary mechanism for encoding information, facilitating signal transmission among diverse neuronal populations ([He & Yang, 2021](#)). The complexity arises from the presence of billions of neurons along with trillions of synapses that govern different functions in the body ([He & Yang, 2020](#)). These neurons form highly intricate and complex connections with each other giving rise to a complicated processing network which governs our thoughts, sensations, actions, and feelings ([Stiles & Jernigan, 2010](#)). They also underlie the brain's remarkable ability to process information, learn from experience, and generate emergent responses. These neural networks are not stable but continuously shaped by different factors such as genetic pathways, brain plasticity, nonlinear kinetics of ion channels, and the dynamic nature of neural networks adding to the complexity of the brain. Central to this complexity is the brain's nonlinearity, characterized by the nonlinear nature of neural signals at the level of individual neurons and their interaction with other networks.

The nonlinear nature in the neuronal responses is reflected in their firing behaviors, which can change in time and frequency domains, contributing to various brain behaviors such as brain plasticity, neural oscillation, and chaotic behavior ([Tsuda, 2001](#)). The interplay between the various factors in the neural network which can change on a variety of time scales are fundamentally nonlinear in the time domain. Furthermore, the nonlinearity in the neural system is viewed in the frequency domain and how fast a neuron can reconfigure its network state rapidly ([Shettigar et al., 2022](#)). Understanding and modeling this nonlinearity is essential for unraveling the brain's complex dynamics which enables the various complex functions of the neural system and emergent responses.

To understand the intricate and complex interactions among the different features of the neurons, computational models have been proposed to replicate their firing behavior. These models provide key insights into the cellular mechanism that governs the initiation and propagation of an action potential. They are designed to meticulously replicate the neuron's morphological and electrical behavior in response to a given stimulus. The morphology and shape of the spikes aids in revealing much of neural dynamics and its relation to the different ionic channels. Therefore, electrophysiological models have been proposed to capture the essential dynamics of the spike. Among these is the Integrate and Fire Model ([Brette & Gerstner, 2005](#)), Izhikevich's spiking neuron model ([Izhikevich, 2003](#)), Morris-Lecar model ([Morris & Lecar, 1981](#)), FitzHugh-Nagumo model ([Sherwood, 2013](#)), Wilson-Cowan model (Wilson, 1972), and Hodgkin Huxley model ([Hodgkin & Huxley, 1952](#)). The Hodgkin Huxley had gained greater attention due to its critical role in describing the electrical behavior of neurons and its biological realism incorporating realistic representation of ionic currents and their interactions. Another significant impact of the model lies in comprehending the role of the different ion channel parameters that control both the timing of each action potential and the frequency of firing encoded in the spike train ([Ranjan et al., 2011](#)). One advantage of this model is the ability to accurately represent each ionic current as a series of mathematical equations, which largely mimics the underlying behavior, accurately fitting the measured data (the neuron's voltage response) to a variety of stimuli. Through the application of this mathematical model to experimentally recorded voltage traces, we can gain insights into the kinetics of the ion channels as well as the neuron's response in healthy and pathological conditions.

Besides the high complexities of modeling nonlinear systems like neuronal systems, identifying the suitable stimulus, or set of stimuli, to perturb the system is a key factor to study the underlying dynamics. Moreover, the absence of a well-defined error function that validates the model by giving an accurate assessment of how close the model simulation is to the biological recording is another hurdle in the way.

The primary challenge in modeling neurons lies in the eclectic electrical behavior which results from the intricate interplay of a large cocktail of ion channels. These components, which are embedded within the neuron's membrane, exhibit unpredicted behavior characterized by time variance, chaotic inputs, and various system interactions. Several studies had been published to illustrate that within the neural dynamical system, several nonlinear interactions between ion channels affects the firing patterns of neurons. Klausberger et al. (2008) illustrate the nonlinear behavior of the GABAergic interneurons within the hippocampus that interfere with the probability of sodium spikes. In particular they found that the firing frequency of perisomatic- and dendrite-targeting interneurons may differentially entrain the output of postsynaptic pyramidal neurons ([Klausberger & Somogyi, 2008](#)).

Another challenge with nonlinear models lies in the fitting process of the mathematical model which is characterized by their sensitivity to initial conditions and parameters, where different parameter configurations can have a profound effect on the spikes' shapes and patterns ([Kumar et al., 2010](#)). This illustrates the importance of parameter selection and estimation in the model fitting process. Additionally, in some mathematical expressions that govern a dynamical system, increasing the number of parameters makes the optimization process more difficult and therefore affecting the

model fit. Therefore, the nonlinearity in most neuronal models can be challenging to analyze and interpret.

The third key factor contributing to the challenges in modeling the brain is the stimuli used to drive the model. When choosing the input to computational model it is important to consider whether this stimulus is effective enough to simulate the whole dynamical range of the neuron. That being said, an effective injected stimuli waveform should have amplitudes large enough ( $\pm$ ) and be applied for a sufficient duration to explore the full range of neuron variations. Additionally, the current should explore all time scales present in the neuron's behavior.

Electrophysiologists use step current to simulate the behavior of neurons; however, simulating a computational model with a step or ramp current is not sufficient to unveil the activation and inactivation kinetics of the different ion channels. Hence, we propose the use of chaotic stimuli which provide opportunities to investigate the complex interactions present in a biological system. Chaotic signals are characterized by their sensitivity to initial conditions (Hollar 2018) and high randomness which makes them valuable in elucidating the behavior of a neuron's dynamics. To the best of our knowledge none of the models proposed in literature used chaotic stimuli to simulate a realistic biophysical model.

Finally, a central challenge in computational neuroscience is finding a well-defined error function that can capture the full complexity of the neural response model. Assessing the effectiveness of neuron models is crucial for their improvement and to understand the complexity of the brain. Therefore, finding appropriate metrics allows for the comparison of various models and the selection of those that most accurately represent the data especially when dealing with models stimulated by complex stimuli. Methods

used in literature focus on specific metrics such as timing or membrane voltage alone; however, an action potential has various features that are critical in interpreting the differences between two models. Choosing the best fit for a model should be done by considering all features of an action potential such as: threshold voltage, amplitude, spikes time, subthreshold oscillation, and frequency. This is illustrated in figure 1. In this paper, Daou et al fitted their model using two criteria: manual fitting and automated parameter search algorithm ([A. Daou & D. Margoliash, 2020](#)). Figure 1a shows a biological recording (blue) for a neuron overlaid by a manual fit while figure 1b shows the same biological trace overlaid by the best fit whose parameters are exhausted by supercomputers. As depicted in figure 1, finding the best fit to such a system requires capturing the different components of the system such as the shape of the response curve, timing of the spikes, minimum and maximum voltage, in addition to other components depending on the system to be analyzed. Thus, it is evident that neither fit fully captures all the features of the system. In such cases, the most effective approach to assess which model truly captures the true data, is through employing an error function capable of evaluating the various model fits of any physiological system. Therefore, criteria for judging the model's performance should be based on the error function used.

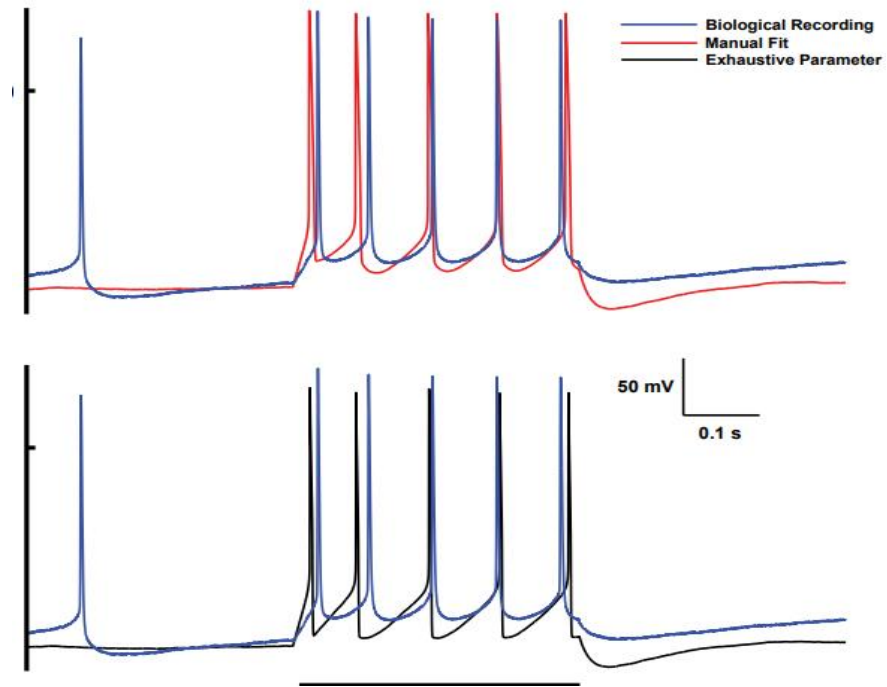


Figure 1: Manual and Automated Fits for Model and Biological Trace

The top panel displays voltage traces from the biological recording (blue) overlaid with those from the manual fit simulation (red). The bottom panel shows overlaid waveforms from the same biological recording (blue) and the best fit from the automated parameter search (black). Both manual and automated fits provided accurate estimates for spike amplitude, frequency, timing, and over all spike shape. ([Daou & Margoliash, 2020](#)).

## B. Criteria for the Evaluation of Proposed Models

Currently there is no gold standard error function that is able to analyze thoroughly and accurately the goodness of a fit in the field of computational neuroscience. The neural responses of a model in literature are often assessed by either the membrane potential ([Asari & Zador, 2009](#)) or as the time-varying firing rate ([Schreiber et al., 2003](#); [van Rossum, 2001](#); [Victor & Purpura, 1996](#)). Below we list several evaluation methods that are used to assess the goodness of a fit.

Spike train distance measures are used to assess the similarity or dissimilarity between two or more spike trains which are a series of action potentials. It aims in creating

a systematic mathematical framework by defining a measure of the distance between a series of spikes ([Houghton & Victor, 2011](#)). An optimal targeted distance is the minimum between the two trains. However, these measures assume that the shape of the action potential and background activity are not relevant, focusing on the spike timing only.

### ***1. Victor and Purpura Method***

Victor and Purpura (1996) focus on finding the minimum cost of transferring one spike train into another using the cheapest way that is by deleting, adding or shifting a spike. This method defines a metric which determines the cost of moving a spike. A parameter  $q$  is used to evaluate the shift in a spike. Figure 2 illustrates an example of two spike trains (X and Y) in which a path is constructed to connect spike X and spike Y. However, in this approach, the first important discovery of the time coding analysis is that, even for parameter values that appear to indicate time coding, the spike-resolved Victor-Purpura distance always compares the spike trains spike for spike. Large spike count disparities prevent spike-resolved distances from being able to evaluate timing information beyond spike pairs; as a result, regardless of the time scale choice, the majority of the distance is frequently caused by mismatches in spike counts rather than timings. Consequently, timing data for the Victor-Purpura distance is only accessible for spike trains with nearly equal rates ([Satuvuori & Kreuz, 2018](#))

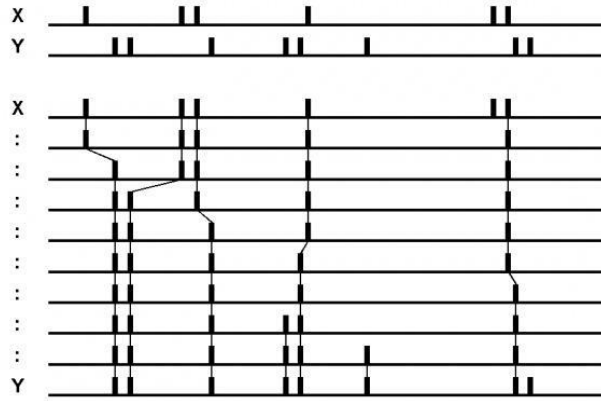


Figure 2: Victor-Purpura Spike Train Distance

Two spike trains X and Y and a path of basic operations (spike deletion, spike insertion, spike shift) transforming the one spike train into the other. Modified from Victor and Purpura, 1996.

## 2. Van Rossum Method

The Van Rossum method assesses the similarity of two spike trains by computing the Euclidean distance of adjusted spike trains with an exponential function ([Zeng et al., 2022](#)). It is represented explicitly as:

Equation 1. Van Rossum method

$$VRD = \sum_i \sum_j e^{-\frac{|u_i - u_j|}{\tau}} + \sum_i \sum_j e^{-\frac{|v_i - v_j|}{\tau}} - 2 \sum_i \sum_j e^{-\frac{|u_i - v_j|}{\tau}}$$

## 3. Schreiber et al. Similarity Measure

The Schreiber similarity measure, proposed by Schreiber et al., quantifies the similarity between spike trains by convolving them with a Gaussian filter to emphasize firing rate patterns. The measure is computed as 1 minus the Pearson correlation coefficient between the convolved spike trains, yielding a value between 0 (no similarity)

and 1 (perfect similarity). This approach is valuable for comparing spike trains with different firing rates or temporal patterns, as it emphasizes underlying firing rate dynamics rather than precise spike timing. However, this method has some limitations: since each spike train is normalized individually before calculating the Schreiber similarity measure, the measure focuses only on similarities in the temporal patterns of firing rates between the two spike trains. It does not consider differences in the overall number of spikes between the two trains. So, if two spike trains have similar firing rate patterns but different overall spike counts, the Schreiber similarity measure may not accurately capture their similarity. Figure 3 illustrates the procedure of transferring spike train X and Y using van Rossum and Schreiber et al (bottom). Each of these methods uses a different metric to convolve the spike times and then calculate the distances differently ([Schreiber et al., 2003](#)).

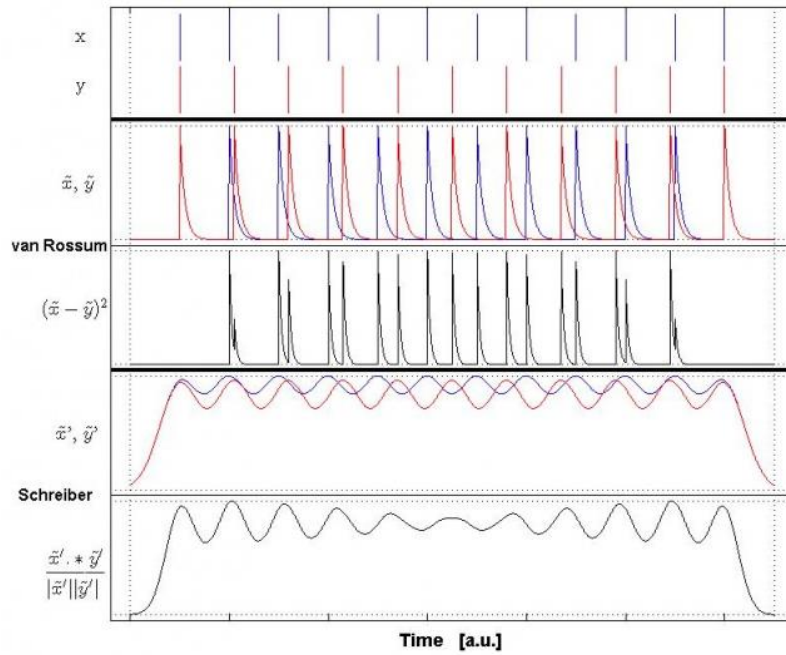


Figure 3: Van Rossum Distance and Schreiber Methods

Illustration of Van Rossum distance and Schreiber methods. Two spike trains X and Y, exponential convolutions, Euclidian difference (van Rossum, 2001), Gaussian convolution and normalized point-wise multiplication (Schreiber et al., 2003).

Where  $u$  is the true spike train and  $v$  is the predicted spike train. The time constant  $\tau$  acts as the parameter that sets the time scale.

This method ties spike timing in a more biologically manner by incorporating a kernel. Each spike is subjected to an exponentially decaying kernel with a time constant, and the distance calculation considers differences in the resulting effect patterns. A larger value corresponds to a longer-lasting effect of a spike. While the profiles generated are dependent on time, there is no normalization with respect to time. Instead, the values are derived on a spike-by-spike basis, as each spike is convolved with a kernel function. This approach results in a distance metric that is spike-resolved, rather than time-resolved. The Victor-Purpura distance and the van Rossum distance are often seen as interchangeable, with a parameter conversion formula of  $1/q$  (Satuvuori & Kreuz, 2018).

The Van Rossum approach has the same limitation as the Victor Purpura: sensitivity to spike timing, dependence on time scale parameter, in addition to normalization issues for different tau-values.

#### 4. *Bivariate SPIKE-distance*

The Spike-distance described by Kreuz et al, is a function that considers both the timing and order of the spikes. It quantifies the distance between two spikes by comparing the time of each spike. The distances between all pairs of spikes are averaged to obtain a comprehensive measure of similarity. This method relies on the instantaneous dissimilarity values that are calculated based on the difference between spikes times. This method produces a Spike-dissimilarity profile  $S(t)$ . The profile is based on three piecewise constant quantities. Each spike is assigned the distance to its nearest neighbor in the second spike (time preceding the spike, time of the following spike, and the instantaneous inters pike interval). These are given by the following equations and illustrated in figure 4 ([Kreuz et al., 2013](#))

Equation 2: Time of Preceding Spike

$$t_p^{(n)}(t) = \max_i (t_i^{(n)} | t_p^{(1)} < t)$$

Equation 3: Time of the Following Spike

$$t_F^{(n)}(t) = \min_i (t_i^{(n)} | t_p^{(1)} > t)$$

Equation 4: Instantaneous Interspike Interval

$$x_{ISI}^{(n)}(t) = t_F^{(n)}(t) - t_p^{(n)}(t)$$

A locally weighted average is used for each spike train, with differences for the closer spike dominating and weighting factors based on

Equation 5: Local Weighted Average

$$x_p^{(n)}(t) = t - t_p^{(n)}(t)$$

and

$$x_F^{(n)}(t) = t_F^{(n)}(t) - t$$

Where  $n$  is the number of the spikes in the spike train and  $I$  is the number of the spike in the  $n^{th}$  spike train.

The instantaneous absolute difference is then calculated as follows:

Equation 6: Instantaneous Absolute Difference

$$\Delta t_p(t) = |t_p^{(1)}(t) - t_p^{(2)}(t)|$$

$$\Delta t_F(t) = |t_F^{(1)}(t) - t_F^{(2)}(t)|$$

Based on these quantities the normalized timescale invariance is obtained:

Equation 7: Normalized Timescale Invariance

$$S'(t) = \frac{\Delta t_p(t) + \Delta t_F(t)}{2 \langle x_{ISI}^{(n)}(t) \rangle}$$

To get a more local time in which the spikes that are closer in time dominates, the weighted average is calculated:

Equation 8: Weighted Average

$$\langle \Delta t_j(t) \rangle_{j=P,F} = \frac{\sum_{j=P,F} \Delta t_j(t) \frac{1}{\langle x_j^{(n)}(t) \rangle_n}}{\sum_{j=P,F} \frac{1}{\langle x_j^{(n)}(t) \rangle_n}}$$

Therefore, the similarity profile is given as follows:

Equation 9: Similarity Profile

$$S_o(t) = \frac{\Delta t_p(t) \langle x_F^{(n)}(t) \rangle_n + \Delta t_F(t) \langle x_P^{(n)}(t) \rangle_n}{\langle x_{ISI}^{(n)}(t) \rangle_n^2}$$

Based on the similarity profile above the bivariate SPIKE-distance is calculated based on the integration over time:

Equation 10: Bivariate SPIKE-Distance

$$D_s = \frac{1}{T} \int_{t=0}^T S(t) dt$$

The SPIKE-distance is within the interval [0,1]. The value zero indicates a perfect spike train.

Unlike many other spike train distance measures, this method is time-resolved ([Kreuz et al., 2013](#)). It can monitor changes in the immediate clustering of spikes by identifying time localized patterns of similarity or dissimilarity among two or more spike trains.

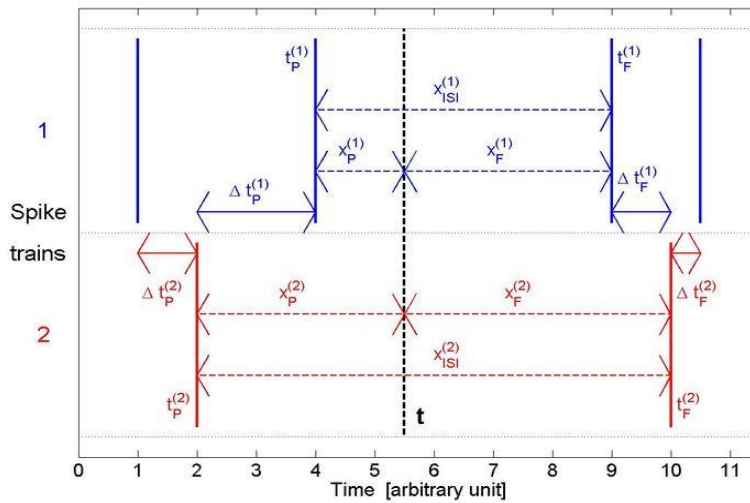


Figure 4: The Bivariate Spike-Distance

Illustration of the local quantities (relative to time instant  $t$ ) needed to calculate the instantaneous dissimilarity values on which the bivariate spike-distance (and its real-time variant) are based. Modified from Kreuz et al., 2013.

## 5. Comparing Spike Potentials

The Root Mean Square Error is a popular method to calculate the mean square for the membrane potential and predicted membrane potential described as follows:

Equation 11: Root Mean Square Error

$$\text{RMSE} = \sqrt{\frac{1}{n} (\sum_{i=1}^n (u_i - u_j)^2)}$$

where  $u_i$  is the experimental voltage of the membrane and  $u_j$  is the model voltage.

Although this approach is one of the popular methods for evaluating the performance of the proposed model, it is limited in capturing the specific timing and pattern of spikes. It only focuses on the overall differences in spike shape. In addition, the root mean square error is highly sensitive to outliers which affects the model's accuracy resulting in misleading interpretation of the model accuracy.

Based on these metrics, it can be argued that they are not sufficient to assess the goodness of a fit in computational neuronal models. They do not fully capture the complex variations of an action potential since they only focus on one feature (time or voltage). However, a single spike holds much more information during initiation and propagation related to: amplitude, duration, frequency, spikes timing, threshold timings, and subthreshold oscillations. Consequently, they might not offer enough details to evaluate how accurately a neuronal model replicate the biological recording of a neuron.

To achieve a more comprehensive assessment, some researchers have focused on using multiple metrics together rather than using one metric. Zeng et al. employed a combination of the two metrics (RMSE, Van Rossum) to evaluate the effectiveness of their proposed model where the RMSE is used to capture the discrepancies in the membrane voltage and Van Rossum method to predict the accuracy of the spike's times.

Given the limitations of existing metrics when used solely, it is important to design a novel error function that analyzes an existing model by considering the different features of a spike. These features are valuable since they are related to the intrinsic properties of the neuron. Thus, targeting the discrepancies in these features allows us to evaluate our model effectively. We will be talking later about the new metrics that we have used in terms of both stimulus presentation and model assessment.

### **C. Hodgkin Huxley Model**

The main objective of conductance-based modeling is the ability to replicate, elucidate, and predict electric activity of neurons and their dynamics. The conductance-based modeling of neuronal excitability was proposed in the 1950s by Hodgkin and Huxley and marked the beginning of analyzing the cellular dynamics of excitability in squid giant axons ([Hodgkin & Huxley, 1952](#)). It reproduces the electric characteristics of neurons by mimicking action potentials, spiking behavior, and ionic channels (Gábor and Banga 2015). The model describes the electrical behavior of the neuronal cell membrane along with voltage gated ion channels that are highly permeable to specific ions.

Figure 5 illustrates the neuronal cell membrane with the ionic channels separating the extracellular and intracellular medium. The medium surrounding the membrane consists of different ions that are involved in the initiation process of an action potential. These electrolytes are  $K^+$ ,  $Na^+$ ,  $Ca^{2+}$ ,  $Cl^-$ , and different neurotransmitters. It also depicts the equivalent electric circuit proposed by the Hodgkin Huxley model where the plasma membrane acts as a capacitor and the ionic channels spanning the phospholipid bilayer act as electrical conductors that depend on voltage and time. According to the Hodgkin Huxley model, the current can be carried through the membrane either by

charging the membrane capacity or by movement of ions through the resistance in parallel with the capacity. The neuronal membrane establishes ion gradient through active transport of ions. This process will allow the establishment of the Nernst Potential for each individual ion channel ( $E_k, E_{Na}, E_L$ ).

Therefore, as per Kirchhoff's Law the current balance equation in the model compartment is described as follows:

Equation 12: Current Balance Equations

$$C_m \frac{dV}{dt} = \sum_k I_k(t) + I_{app}$$

Where  $C_m$  is the membrane capacitance,  $V_m$  is the intracellular potential,  $I$  is the corresponding current for the  $k$ th ionic channel,  $I_{app}$  is the applied current.

The model describes different types of ionic channels based on their unique dynamics and the flow of ions through it. The generation of action potentials, along with their shape and firing patterns, depends in large part on voltage gated sodium  $Na^+$ , and potassium  $K^+$ , channels and their kinetics (Berger and Crook 2015).

The key insight of the Hodgkin Huxley model is the development of a model in which the properties of an excitable cell are described by a set of ordinary differential equations. These equations describe in detail the initiation of action potentials in neuron cells, as a result of complex exchange of ionic species between the outer and inner part of the membrane. Through this ionic exchange, neurons integrate ionic signals over time, and this alters the membrane potential. The differential equations are governed by activation and inactivation kinetics that allows the membrane to self-regulate and modulate its activity by opening or closing in response to a stimuli (Bähring and Covarrubias 2011).

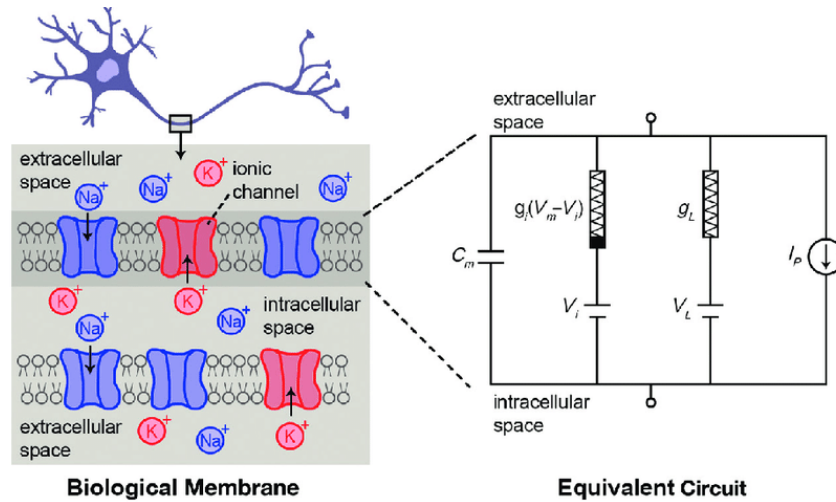


Figure 5: Hodgkin–Huxley Model of Biological Neurons

The model describes in detail the initiation/temporal response of action potentials in biological cells—illustration of a neuronal biological membrane. On the right the equivalent electric circuit that is proposed Hodgkin–Huxley model.

#### D. Data Assimilation

In this study we focus on data assimilation techniques which will allow us to capture the complex dynamics by adjusting the model’s parameters. Data assimilation is a mathematical model that describes analytical and numerical techniques through which information from measurements is incorporated into selected dynamical equations of a model. This approach is especially important when dealing with chaotic nonlinear systems and noisy data which is the case with neural dynamical systems. Such systems are highly sensitive to initial conditions posing a challenge to predict their response accurately. Therefore, to address this, it is essential to continually adjust the trajectory based on observed systems states which is the main objective of data assimilation. This technique involves effectively combining observations from a system to enhance estimates of a model output that describes the system. Thus, data assimilation allows us to determine the parameters of the model and the temporal evolution of unobserved state variables. It tends to estimate how different parts of a network are connected and to

determine the complete state of the model at the end of a period where observations are made and used to refine the model. During this period, the measurements update the model's initial conditions, and the model's behavior can be projected into the future. This helps in evaluating whether the model accurately represents the underlying processes that generate the observations. Once validated, the model can be used to predict how the network will respond to new inputs or changes ([Abarbanel et al., 2018](#)).

In order to implement this model, we need three requirements: observations (data or measurement model), a background (priori state or process model) ,and information about the distribution of the errors on these two ([Amendola et al., 2020](#)).

To start with, consider the mathematical model described by differential equation as shown below:

Equation 13: Differential Equation Describing the Model

$$\frac{dx_a(t)}{dt} = F_a(x(t), q),$$

$$x_a(t_n + 1) = x_a(n + 1) = f_a(x(t_n), q) = f_a(x(n), q)$$

Where  $x$  represents the state of the system and  $q$  is a set of fixed parameters.

This differential equation can also be replaced by Hodgkin Huxley model.

Using this approach, the parameter  $q$  and the state of the system at the end of the observation window can be determined.

We take an observation window between  $t_o$  and  $t_f$   $[t_o, t_f]$ . We perform a set of measurements within this interval  $t = \{\tau_1, \tau_2, \dots, \tau_k, \dots, \tau_F, \}; t_o \leq \tau_k \leq t_f$ . At each of these measurement times, we collect  $L$  quantities  $y(\tau_k) = \{y_1(\tau_k), y_2(\tau_k), \dots, y_L(\tau_k)\}$ . The number  $L$  of observations at each measurement time  $\tau_k$  is typically less, often much

less, than the number of degrees of freedom  $D$  in the observed system;  $D \gg L$ . (Miller et al., 2018).

After collecting observations, we proceed with the second step by using the model dynamics.

Using the equation above, we step the model variables from  $t_0$  to  $\tau_1$ , then from  $\tau_1$  to  $\tau_2$  and so on until reaching  $\tau_F$ . We then move the model from  $x(\tau_F)$  to  $x(t_F)$ .

This involves iterating the model equations multiple times with a time step  $\Delta t$  to accurately represent the model dynamics.

The set of model states at each time point  $t_n$  is collected into a path through a  $D$ -dimensional space, is denoted as  $X = \{x(0), x(1), \dots, x(n), \dots, x(N) = x(F)\}$ . This path represents the evolution of the model state over time.

So now we collected two essential components for the transfer of information: measurement data ( $Y$ ) represented:  $Y = \{y(\tau_1), y(\tau_2), \dots, y(\tau_F)\}$  and model-based knowledge represented by  $f_a(x(n), q)$ .

Figure 6 illustrates a visual representation of the time window during which observation of variable  $Y$  are taken.

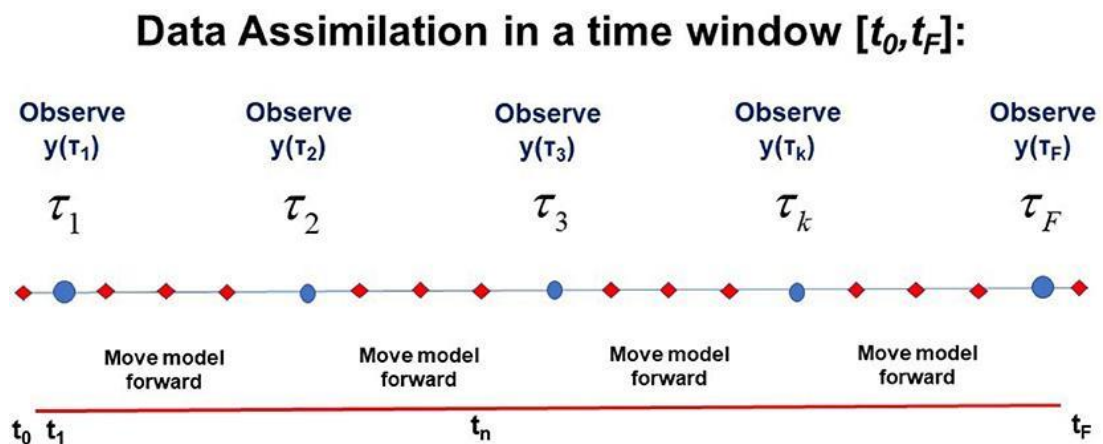


Figure 6: Data Assimilation Method

A visual representation of the window  $t_o \leq \tau_k \leq t_f$  in time during which L-dimensional observations  $Y(\tau_k)$  are performed at observation times  $t = \tau_k$ ;  $k = 1, \dots, F$ . This also shows times at which the D-dimensional model developed by the user  $x(n+1) = f(x(n), q)$  is used to integrate forward from time  $n$  to time  $n+1$ :  $t_n = t_o + n\Delta t$ ;  $n = 0, 1, \dots, N$ .  $D \geq L$ . The trajectory of the model  $X = x(0), x(1), \dots, x(n), \dots, x(N) = x$  and the collection  $Y$  of L-dimensional observations at each observation time  $\tau_k = \{\gamma(\tau_1), \gamma(\tau_2), \dots, \gamma(\tau_F)\}$   $Y = \{y_1, y_2, \dots, y_L\}$  is also indicated. Extracted from ([Miller et al., 2018](#))

The third requirement for this process of transferring information from measurements to a model is compromised of the methods used to make this transfer. The success of these methods can be evaluated based on how well they predict the properties of the model at the measurement times  $\tau_k$  where the model variables  $x(0)$  associated with  $Y(\tau_k)$  are close to  $Y(\tau_k)$ . However, merely achieving consistency with the known data at measurement times is not sufficient. The model, along with estimates of its parameters  $q$  and its state at the final time  $t_f$ ,  $x(t_f)$  must also be used to predict future values for  $t_f$ . These predictions should match measurements made at times  $\tau_r > t_f$ . The success of these predictions can be evaluated using the same metric as used in the observation window ([Miller et al., 2018](#)).

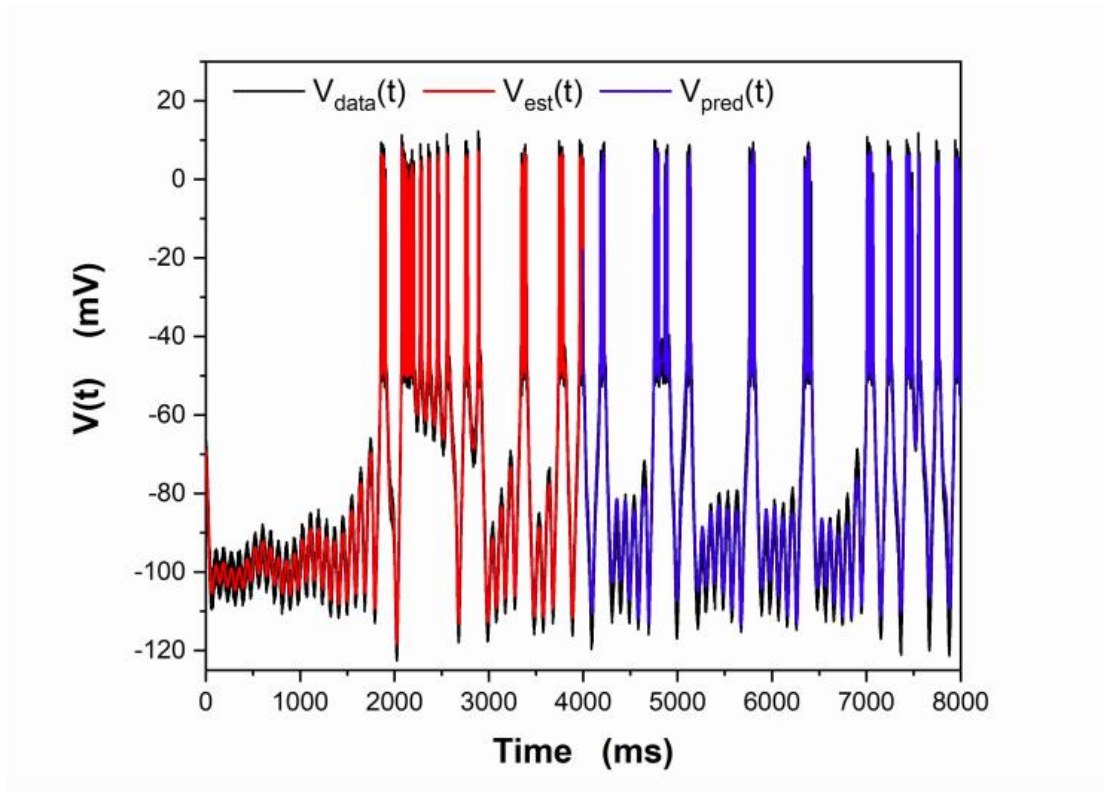


Figure 7: Data Assimilation Applied to the Noisy Data (Voltage and Injected current).

The noisy model voltage data is shown in black, and the estimated voltage is shown in red. For  $t \geq 4,000$ ms the predicted membrane voltage, in blue, is generated by solving the model equations using the parameters estimated during statistical data assimilation within the observation window ([Miller et al., 2018](#)).

**Figure 7** illustrates the data assimilation methodology which shows *three* windows: observed window, estimated, and predicted. In their paper Miller et al., utilized the data assimilation method to a basal ganglion projecting neuron in the avian song system. They constructed their model by varying some parameters related to the ion channels within the first-time interval of 4 seconds. They then performed estimates to the different parameters in the system Beyond that they assessed the accuracy of their numerical predictions by comparing them to the actual data. The outcome of this procedure can be seen in figure 4. The waveform represents two traces: Biological trace (black) and model trace (red and blue). During the first set of measurements (0 till

4000ms) a set of parameters is regularly updated until a good fit is acquired which is overlaid on the synthetic input data in black. Beyond that the parameters obtained during the interval of  $t < 4000\text{ms}$  are used to generate the predicted voltage trace. Their method show that the red curve matched the computed voltage curve well.

## CHAPTER III

### RESEARCH GAP

In this study we aim to optimize neuronal fits by modifying the traditional Hodgkin Huxley model to capture the true dynamics of neurons and how different stimulus type influence fitting performance. First, we aimed in modifying the HH model such that it captures the complex heuristics of spike waveforms, especially given the different stimuli. Traditional HH model often struggle to capture the different discrepancies in neuronal model fits associated with the different spike features. Neuronal modeling approaches prioritize spike timing accuracy, assessing model performance primarily through spike-time metrics while neglecting the intrinsic morphological properties of each action potential. This limits our ability to model neuron's activity effectively. To address this limitation, we incorporated neuron-specific tuning of channel kinetics that allow us to reproduce decent fits with improved morphology. This modification can be applied to any spiking neuron in the nervous system. Second, we investigated the effect of changing the type of stimulus on the fitting performance of the model. The type and temporal structure of the stimulus applied to biological neurons significantly influence the observed firing patterns and spike morphology. Therefore, we utilized a set of chaotic stimuli to be given as an input to our neurons in patch clamp configuration (intracellular data collection methodology). The stimuli are being applied to biological neurons in the cortex of zebra finches at the University of Chicago and as a result we will perform our analysis on a dataset where neurons have seen a new class of chaotic stimuli. Traditional input currents such as step or ramp currents are unable to adequately elucidate the different kinetics of ion channels. The effectiveness of a stimuli

should be evaluated based on its ability to constrain the range of model parameters, leading to accurate replication of neuron dynamics. Thus, it is essential to choose a stimulus that can unravel the whole neuronal dynamics and fills the phase space of this dynamical system. This phase space is defined as the space in which all possible states of the dynamical system are present. Step currents tend to stabilize and relax to their limiting stable manifolds while chaotic stimuli will always push the system to a more variable unstable state which resembles the true complexity of neuronal connections. We also developed an analysis method that evaluates individual spikes by comparing their timing and morphology between a modeled trace and a biological trace. The code we developed identifies spikes that are aligned and penalizes missed spikes, extract the different features of the spike (threshold, spike timing, subthreshold oscillation, amplitude, time to peak), and calculate the error between each feature of the model and the biological trace. This code provides a detailed examination of spike timing accuracy and morphology similarity between the model and the biological data. Based on the extracted features and their associated errors we can identify the best fit. Through these tools, we aim to provide a more realistic and predictive neuronal model.

# CHAPTER IV

## METHODOLOGY

The chapter provides the methodology employed to simulate our model along with the procedure of modifying of the HH model and simulation. We first present the model fitting procedures followed by the model input. We provide a thorough explanation of our feature error extraction.

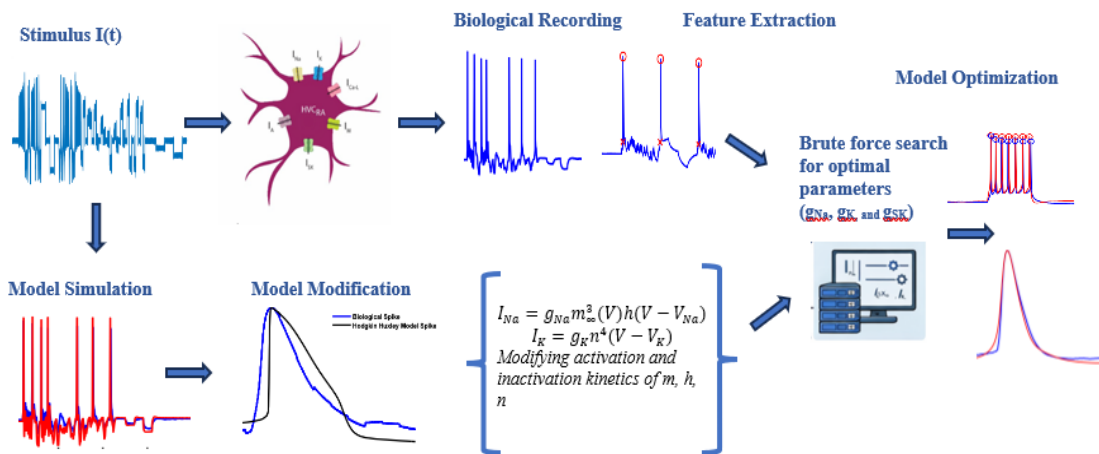


Figure 8: Workflow of the Methodology.

A pseudo-noisy stimulus  $I(t)$  is delivered to biological HVC neurons to elicit electrophysiological responses. Key spike features are extracted from the resulting voltage traces and serve as targets for model optimization. A conductance-based Hodgkin–Huxley framework is refined by tuning channel kinetics and maximal conductances, while extensive parameter-space exploration is carried out using high-performance computing. The resulting optimized models faithfully reproduce spike timing and action potential shape, producing neuron-specific parameter sets that closely match the experimental data the workflow results in an optimized model where the simulated model trace (red) matches the biological trace (blue) in spike timing and morphology.

## A. Hodking Huxley Model Fitting

In this study we utilized a single-compartment conductance-based Hodgkin-Huxley model for  $HVC_x$  neurons, to assess the magnitude of the ionic current. The model consists of different ionic currents including spike producing currents (  $I_k$  and  $I_{Na}$  ) a small conductance  $Ca^{2+}$  activated  $K^+$  current  $I_{SK}$  , a high threshold L- type  $Ca^{2+}$  current  $I_{Ca-L}$  , a low threshold T-type  $Ca^{2+}$  current (  $I_{Ca-T}$  ), a persistent  $Na^+$  current  $I_{Nap}$  , a  $Na^+$ - dependant  $K^+$  current  $I_{KNa}$ , A – type  $K^+$  current  $I_A$ , a hyperpolarization- activated cation current  $I_h$ , and a leak current  $I_L$ .

The model is represented by the following equation:

Equation 14: Membrane Voltage Equation (Current Balance Equation)

$$C_m \frac{dV}{dt} = -I_L - I_k - I_{Na} - I_{SK} - I_A - I_{Ca-L} - I_{Ca-T} - I_{KNa} - I_h + I_{app}$$

The details of the model equations, parameter ranges, and simulation protocol are described below.

## B. Defining the Ionic Channels

The voltage dependent currents of the different ionic channels in this model were modeled according to the following equations:

### 1. Leak Current

Equation 15: Leak Current

$$I_L = g_L(V - V_L)$$

Where  $g$  represents the constant conductance and  $V$  and  $V_L$  represent the reversal potential of ions involved and  $V$  being the membrane potential respectively.

The leakage channel is described by the voltage independence conductance. It is an essential ion channel that determines the input resistance of neurons and indirectly the strengths of synaptic potentials ([Catterall et al., 2012](#)).

All other currents involved in the Hodgkin Huxley model are characterized by their voltage dependence and represented by the following first order differential equation:

$$I = g x_{\infty} h(V - E)$$

$$\text{Where } x_{\infty}(V) = \frac{1}{1 + \left(\frac{V - \theta_x}{\sigma_x}\right)^2} \quad x = m, mp, a, \text{ or } s$$

Where  $\theta_x$  is the half activation voltage for gating variables and  $x = m, mp, a, \text{ or } s$  and  $\sigma_x$  is the slope factor for  $\theta_x$ .

Each gating variable is represented by a first order kinetic equation where the transition rates describe how quickly a channel open or close in response to membrane potential.

## 2. Sodium Ionic Channels

The voltage dependent current of  $I_{Na}$  is given as follows:

Equation 16: Sodium Current

$$I_{Na} = g_{Na} m_{\infty}^3(V) h(V - V_{Na})$$

Where  $g$  is the maximal conductance of the ionic channel,  $m$  being the activation gating variable, and  $h$  is the inactivation gating variable. In classical models, the sodium channels are activated rapidly therefore  $m$  is assumed to reach its equilibrium instantaneously (ref) The spike producing current  $Na^+$  mainly facilitate the rapid increase in membrane potential during initiation of action potential ([Liu et al., 2012](#)). These channels affect the shape and the spiking frequency of a spike train. Increasing this current

leads to an increase in amplitude of the action potential and upward slope. Additionally, increasing  $I_{Na}$  can shorten the interspike interval and increases the spiking frequency ([Milescu et al., 2010](#)).

### 3. Potassium Ionic Channel $I_K$

Equation 17: Potassium Current

$$I_K = g_K n^4 (V - V_K)$$

Where  $n$  is a gating variable given as follow:

$$\frac{dn}{dt} = \frac{n_\infty(V) - n}{\tau_n}$$

where  $\tau_n$  is

$$\tau_n = \frac{\overline{\tau_n}}{\cosh\left(\frac{V - \theta_x}{2\sigma_x}\right)}$$

The spike producing  $K^+$  currents contribute to the repolarization phase by helping to restore the membrane potential.

### 4. Persistent $Na^+$ Current

Equation 18: Persistent Sodium Current

$$I_{Nap} = g_{Nap} mp_\infty(V) h(V - V_{Na})$$

Equation 19: Boltzmann Steady-State Activation of  $I_{Nap}$

$$mp_\infty = \frac{1}{1 + \exp\left(\frac{V - \theta_{mp}}{\sigma_{mp}}\right)}$$

Equation 20: Steady- State Inactivation Function for Sodium Channels

$$h_\infty(V) = \frac{\alpha_h(V)}{\alpha_h(V) + \beta_h(V)}$$

Equation 21: Voltage-Dependant Sodium Inactivation Rate( Forward rate)

$$\alpha_h = 0.128 \exp\left(\frac{V + 50}{18}\right)$$

Equation 22: Voltage-Dependant Sodium Inactivation Rate (Backward Rate)

$$\beta_h = \frac{4}{1 + \exp\left(\frac{-(V + 27)}{5}\right)}$$

Persistent sodium current  $I_{Nap}$  alters neuronal firing behavior by amplifying spike afterhyperpolarization and increasing the regularity of repetitive firing ([Stafstrom, 2007](#)). Its inactivation plays a crucial role in generating the pacemaker potential for the oscillations.

### 5. A – type $K^+$ Current $I_A$

Equation 23: A – type  $K^+$  Current

$$I_A = g_A a_\infty(V) e(V - V_K)$$

Equation 24: Boltzmann Activation of  $I_A$

$$a_\infty = \frac{1}{1 + \exp\left(\frac{V - \theta_a}{\sigma_a}\right)}$$

Equation 25: First - Order Inactivation Dynamics of the A-type Potassium Current

$$\frac{de}{dt} = \frac{e_\infty(V) - e}{\tau_x}$$

The time constant is given as a constant and provided in Table.

The A – type  $K^+$  current produces a delay in spiking and decreases the firing frequency.

### 6. High Threshold L- Type $Ca^{2+}$ Current

Equation 26: High Threshold L- Type  $Ca^{2+}$  Current

$$I_{CaL} = g_{Ca} V s_\infty^2(V) \left( \frac{Ca_{ex}}{1 - \exp\left(\frac{2FV}{RT}\right)} \right)$$

Equation 27: Steady-State Activation Function of the L-type Calcium Current

$$s_{\infty} = \frac{1}{1 + \exp\left(\frac{V - \theta_s}{\sigma_s}\right)}$$

The term  $\frac{F}{RT}$  is the thermal voltage, where T is the temperature of the bathing solution (25°C or 298 K), R is the gas constant, and F is Faraday's constant.  $Ca_{ex}$  is the external  $Ca^{2+}$  concentration, which is 2.5 mM in the bathing solution. The high threshold L- type  $Ca^{2+}$  current induce burst firing.

### 7. Low Threshold T-type $Ca^{2+}$ Current

The expression of Low voltage gated T- type  $Ca^{2+}$  current is expressed as follows:

Equation 28: Low Threshold L- type  $Ca^{2+}$  Current

$$I_{Ca-T} = g_{Ca-T} V [a_T]_{\infty}^3 (V) [b_T]_{\infty}^3 (r_T^A) \left( \frac{Ca_{ex}}{1 - \exp\left(\frac{2FV}{RT}\right)} \right)$$

The activation gating for the rapidly activating channel  $a_T$  is treated as instantaneous and is represented as follows:

Equation 29: Steady-State Activation Function of the T-type Calcium Current

$$a_{T\infty} = \frac{1}{\left(1 + e^{\left(\frac{V - \theta_{aT}}{\sigma_{aT}}\right)}\right)}$$

The inactivation variable ( $[b_T]$ ) is also treated as instantaneous and depends on the slowly operating variable  $r$ , which reflects the availability of the  $I_{Ca-T}$  current. This is represented by:

Equation 30: Inactivation Function of the T-type Calcium Current

$$b_{T\infty}(r_T) = \frac{1}{1 + \exp\left(\frac{(r_T - \theta_b)}{\sigma_b}\right)} - \frac{1}{1 + \exp\left(\frac{-\theta_b}{\sigma_b}\right)}$$

The slowly operating variable  $r_T$  is given by:

Equation 31: Slowly Recovery Dynamics of T-type Calcium Current

$$\frac{dr_T}{dt} = \frac{r_{T\infty}(V) - r_T}{\tau_{r_T}(V)}$$

$$r_{T\infty} = \frac{1}{1 + e^{\left(\frac{V - \theta_{r_T}}{\sigma_{r_T}}\right)}}$$

And

Equation 32: Steady-State Recovery Function of the T-type Calcium Current

$$\tau_{r_T}(V) = \tau_{r_0} + \frac{\tau_{r_1}}{1 + e^{\left(\frac{V - \theta_{r_T}}{\sigma_{r_T}}\right)}}$$

The low threshold T-type  $Ca^{2+}$  current plays a role in rebound burst firing and subthreshold oscillations.

### 8. *Small Conductance $Ca^{2+}$ Activated $K^+$ Current $I_{SK}$*

The  $I_{SK}$  current is modeled as:

Equation 33: Small Conductance  $Ca^{2+}$  Activated  $K^+$  Current

$$I_{SK} = g_{SK} k_{\infty}([Ca^{2+}]_i)(V - V_K)$$

Where  $k_{\infty}([Ca^{2+}]_i)$  is the steady-state activation function of the SK current that is based on the levels of intracellular calcium and is governed by:

Equation 34: Steady-State Activation Function of the SK Current

$$k_{\infty}([Ca^{2+}]_i) = \frac{[Ca^{2+}]_i^2}{[Ca^{2+}]_i^2 + k_s^2}$$

The constant  $k_s$  is the dissociation constant of the  $Ca^{2+}$  dependent current, and  $[Ca^{2+}]_i$  is the intracellular concentration of free  $Ca^{2+}$  ions and is given by:

Equation 35: Dissociation Constant of the  $Ca^{2+}$

$$\frac{d[Ca^{2+}]_i}{dt} = -f \{ \varepsilon(I_{Ca-L} + I_{Ca-T}) + k_{Ca}([Ca^{2+}]_i - b_{Ca}) \}$$

The constant  $f$  represents the fraction of free-to-total cytosolic  $Ca^{2+}$ , whereas the constant  $\varepsilon$  combines the effects of buffers, cell volume, and the molar charge of calcium. The constant  $k_{Ca}$  is the calcium pump rate constant, and  $b_{Ca}$  represents the basal level of  $Ca^{2+}$ .

This type of current is activated by calcium influx through voltage-gated calcium channels during action potential. Once activated these channels mediate hyperpolarization which reduces the firing frequency of neurons ([Louise Faber, 2009](#)).

### 9. Hyperpolarization- Activated Cation Current $I_h$

The  $I_h$  current is modeled as:

Equation 36: Hyperpolarization- Activated Cation Current

$$I_h = g_h[k_r r_f + (1 - k_r)r_s](V - V_h)$$

The fast activation components is governed by:

Equation 37: Fast Activation Components

$$\frac{dr_f}{dt} = \frac{r_{f\infty}(V) - r_f}{\tau_{r_f}(V)}$$

$$r_{f\infty} = \frac{1}{1 + e^{\left(\frac{V - \theta_{r_f}}{\sigma_{r_f}}\right)}}$$

The time constant  $\tau_{r_f}$  is expressed by:

Equation 38: Time Constant

$$\tau_{r_f}(V) = \frac{P_{r_f}}{\frac{-7.4(V + 70)}{e^{\left(\frac{V+70}{-0.8}\right)-1}} + 65e^{\left(\frac{V+56}{-23}\right)}}$$

Equation 39: Slow Activation Component

$$\frac{dr_s}{dt} = \frac{r_{s\infty}(V) - r_s}{\tau_{r_s}}$$

$$r_{s\infty}(V) = \frac{1}{1 + e^{-\left(\frac{V - \theta_{r_s}}{\sigma_{r_s}}\right)}}$$

The time constant  $\tau_{r_s}$  is given in the table.

The hyperpolarization- activated cation current  $I_h$  plays a vital role in establishing the resting membrane potential of neurons and they serve as a mechanism that prevents neurons from becoming overly hyperpolarized ([Ludwig et al., 1998](#)).

Table 1: Constant Parameter Values Used in All Simulations.

Parameter	Value	Parameter	Value	Parameter	Value
$V_L$	-70 mV	$\theta_{r_f}$	-105 mV	$\theta_e$	-40 mV
$V_K$	-90 mV	$\theta_{r_s}$	-105 mV	$k_{Ca}$	$0.3 \text{ ms}^{-1}$
$V_{Na}$	-30 mV	$\theta_{a_T}$	-65 mV	$b_{Ca}$	$0.1 \mu M$
$V_H$	-30 mV	$\theta_b$	0.4 mV	$k_s$	$0.5 \mu M$
$g_L$	2 nS	$\theta_{r_{rT}}$	-67 mV	$K_p$	15 mM
$g_{Ca-L}$	20 nS	$\sigma_m$	-5 mV	$p_{r_f}$	100
$g_{Nap}$	1 nS	$\sigma_n$	-5 mV	$\theta_a$	-20 mV
$\bar{\tau}_n$	10 ms	$\sigma_s$	-0.05 mV	$\varepsilon$	$0.0015 \text{ pA}^{-1} \cdot \mu M \cdot \text{ms}^{-1}$
$\bar{\tau}_{hp}$	1,000 ms	$\sigma_{mp}$	-6 mV		
$\tau_e$	20 ms	$\sigma_{hp}$	6 mV		
$\tau_h$	1 ms	$\sigma_a$	-10 mV		
$\tau_{r_s}$	1,500 ms	$\sigma_e$	5 mV		
$\tau_{r_0}$	200 ms	$\sigma_{r_f}$	5 mV		
$\tau_{r_1}$	-35 mV	$\sigma_{r_s}$	25 mV		
$\theta_m$	-35 mV	$\sigma_{a_T}$	-7.8 mV		
$\theta_n$	-30 mV	$\sigma_b$	-0.1 mV		
$\theta_s$	-20 mV	$\sigma_{r_T}$	2 mV		
$\theta_{mp}$	-40 mV	$\sigma_{r_{rT}}$	2.2 mV		
$\theta_{hp}$	-48 mV	$f$	0.1		

## 10. Channel Gating Dynamics

In classical HH models, the sodium and potassium activation and inactivation variables  $m$ ,  $n$ , and  $h$  are assumed to adjust instantaneously to their steady-state value  $x_\infty$  ([Song et al., 2009](#)). The voltage dependence of the gating variables is described using

empirical functions fitted to voltage-clamp recordings, with parameter values originally obtained from experimental measurements axons ([Hodgkin & Huxley, 1952](#)).

Although the above formulations are widely, in our model we adopted a rate-based Hodgkin–Huxley approach to preserve channel kinetics and allow gating time constants to emerge from voltage-dependent transition rates. Rather than relying solely on the key parameters of the maximal ionic conductance to optimize neuronal model fits we reformulated the gating variables and explored their parameter space.

First to produce membrane trajectories that fit the biological trace, we manually fitted several parameters that directly influence the spikes shape. We adjusted the maximal conductance of the spike producing currents and the small conductance  $Ca^{2+}$  activated  $K^+$  channels ( $g_{Na}, g_K, g_{SK}$ ). These parameters affected different features of the action potentials: firing frequency, spikes time, subthreshold oscillations but failed to capture the accurate morphology of the spikes. Therefore, we modified the classical Hodgkin Huxley model particularly the sodium and potassium kinetics. The interaction between these channels shapes the action potential in the model. Therefore, we examined the kinetics parameters of the gating variables related to these ionic channels in details.

a. Sodium Modified Model

The  $m$  gating variable in eq (1) represents the proportion of ion channels that are activated at the intracellular membrane surface (HH 1952). In our model we modified  $m$  equation as a differential equation rather than an instantaneous one depending on voltage and time:

Equation 40: Fast Sodium Channel Activation Gating Equation

$$\frac{dm}{dt} = \alpha_m(1 - m) - \beta_m$$

The parameters  $\alpha_m$  and  $\beta_m$  refer to the rate constants and are modeled as follow:

Equation 41: Voltage-Dependent Sodium Activation Rate Constant.

$$\alpha_m = k_{1m} * \frac{(V + k_{2m})}{1 - \exp(\frac{-(V + k_{2m})}{k_{3m}})}$$

Equation 42: Voltage-Dependent Sodium Deactivation Rate Constant

$$\beta_m = 4 \exp(-0.0556 * (V + k_{4m}))$$

The h gating variable refers to the inactivation of the sodium channels when the membrane

depolarizes. The variable h is modeled as a differential equation shown below:

Equation 43: Fast Sodium Channel Inactivation Gating Equation

$$\frac{dh}{dt} = \alpha_h(1 - h) - \beta_h$$

Equation 44: Steady-State Inactivation Function of the Sodium Channel

$$h_\infty(V) = \frac{\alpha_h(V)}{\alpha_h(V) + \beta_h(V)}$$

Equation 45: Voltage-Dependent Sodium Inactivation Rate Constant

$$\alpha_h = 0.128 \exp(\frac{V + k_{5h}}{k_{6h}})$$

Equation 46: Voltage-Dependent Sodium Recovery Rate Constant

$$\beta_h = \frac{4}{1 + \exp(\frac{-(V + k_{7h})}{k_{8h}})}$$

our model, only a subset of parameters was varied. The numerical constants  $-0.0556$  and  $4$  in the  $\beta_m$  equation were kept fixed, as modifying them did not substantially alter the shape of individual action potentials but instead affected overall spike-train excitability. In contrast, parameters  $k_{1m}$ - $k_{8h}$  directly influenced action potential morphology and were therefore varied to capture differences in spike shape.

The parameters  $k_{1m}$ – $k_{4m}$  represent intrinsic channel-kinetic properties of the  $m$  gating variable related to the sodium channel regulating the rate constants (and thus the morphology of the action potential).  $k_{1m}$  represents a scaling factor for the activation kinetics of the  $m$  gating variable. This factor highly affects the speed at which the sodium channels open. Increasing  $k_{1m}$  causes the sodium channels to open rapidly. We constrained the values of  $k_{1m}$  between 0.05 and 0.1.

$k_{2m}$  refers to the voltage offset which is a fixed parameter applied in the model equations to adjust the voltage range over which the gating variables  $m$  activates (ref). Decreasing  $k_{2m}$  to a more negative value displaces sodium channel activation toward higher membrane voltages, leading to an elevated spike threshold and decreased neuronal excitability. Therefore, for  $k_{2m}$  we chose a range between 35 and 50 with increments of 5. Increasing  $k_{2m}$  to a value beyond 50 will trigger unrealistic behavior of the neuron.

$k_{3m}$  is the slope factor of the curve controlling the voltage sensitivity of therefore we constrained the values between 8 and 20.  $k_{4m}$  represents the offset of the sodium activating gating variable, thereby influencing the rate at which the sodium activation gate closes in the rising phase. We varied the values of  $k_{4m}$  between 30 and 80 with increments of 80. These parameters shape the rising phase of the action potential.

The inactivation of the sodium channels is shaped by the  $h$  gating variable. The rate constant  $\alpha_h$  controls how quickly sodium channels recover from inactivation, while  $\beta_h$  controls how rapidly sodium channels enter the inactivated state. Of The parameters  $k_{5h}$ ,  $k_{6h}$ ,  $k_{7h}$  and  $k_{8h}$  shape the inactivation function of the sodium channel.  $k_{5h}$  represents voltage offsets that shift the voltage dependance of the channel recover from inactivation left or right. We constrained the values of  $k_{5h}$  between 40 and 80 with increments of 10.  $k_{6h}$  is the voltage sensitivity and thus affecting how steeply  $\alpha_h$  change

with voltage. The values of  $k_{6h}$  are chosen between 10 and 20 with increments of 5. Similarly,  $k_{7h}$  and  $k_{8h}$  affect  $\beta_h$  where  $k_{7h}$  is the voltage offset that shifts the voltage range at which inactivation is initiated while  $k_{8h}$  is voltage sensitivity thus affecting how sharply this transition occur. The values of  $k_{7h}$  were chose to vary between 24 and 28 with increments of 2 while that of  $k_{8h}$  are between 4 and 10 with increments of 1.

b. Modified Potassium Kinetics

Equation 47: Voltage-Dependent Potassium Activation Rate Constant

$$\theta_n = \frac{k_9 \times (v + k_{10})}{1 - \exp\left(\frac{-(v + k_{10})}{k_{11}}\right)}$$

Equation 48: Voltage-Dependent Potassium Deactivation Rate Constant

$$\beta_n = 0.125e^{-\left(\frac{v+k_{12}}{k_{13}}\right)}$$

The same procedure is applied to the potassium channels. The n gating variable represents activation variable of the potassium channels with rate constants of  $\theta_n$  and  $\beta_n$ .  $k_{9n}$ ,  $k_{10n}$ , and  $k_{11n}$  shape the opening of the potassium channels while  $k_{12n}$  and  $k_{13n}$  shape the closing of the channels. In particular,  $k_{9n}$  is a rate scaling constant that affects how fast the potassium channel opens. Increasing  $k_{9n}$  allows more  $K^+$  current to flow outward causing stronger hyperpolarization and harder rebound. We varied this parameter using small increments, as even a minimal change (e.g. 0.001) can produce a large effect in the negative regime. Therefore, we chose parameters between 0.005 and 0.02 with increments of 0.001.

$k_{10n}$  and  $k_{11n}$  refer to the voltage offsets of potassium activation channel while opening. The range of  $k_{10n}$  were varied between 30 and 50 with steps of 5  $k_{11n}$  is between 8 and 14 with steps of 2.  $k_{12n}$  and  $k_{13n}$  shape the closing of the potassium channels.  $k_{12n}$  is also a voltage offset and was varied between 30 and 50 with increments of 5. As for increasing  $k_{13n}$  makes the potassium more negative and thus pushing it to the more hyperpolarized region so we constrained parameters between 35 and 55 with increments of 10.

The overall equation of each of the activation and inactivation kinetics of the gating variables regulate the shape of the action potential and thus increasing or decreasing any of these parameters has a great impact on the spike morphology. These parameters all together act as knobs that regulate the shape of the action potential.

Therefore, to find their appropriate values we ran an exhaustive brute force search on each parameter and checked their contribution to the overall shape of the action potential. We developed a MATLAB pipeline that proceeds in two stages.

First, we systematically varied the key parameters ( $g_{Na}$ ,  $g_K$ ,  $g_{SK}$ ) to obtain a set of parameter combinations that produced reasonable fits to the experimental data. Once satisfactory fits were achieved for these conductance's, we subsequently refined the model by varying the gating-variable parameters ( $k_1 \dots k_{12}$ ) defined above.

The MATLAB code takes the applied current as input and numerically integrates the model while varying the  $k_1 \dots k_{12}$  parameters. For each neuron, a large-scale brute-force parameter search was performed on a high-performance computing (HPC) cluster due to the high dimensionality of the parameter space. At each iteration, we extracted the first action potential generated by the model and compared it to the corresponding biological spike by computing the mean squared error. We then stored each parameter

set, together with its associated error value for subsequent analysis. Given the huge data sheet we had, we searched for the minimum squared error value and then used these parameters set to fit the whole spike train. We applied this to neurons of which we had decent fits.

### **C. Model Input**

In the next part of our model, we will be using the Pseudo noisy stimuli which consists of various chaotic currents that will incorporate the complex dynamics of neurons. We generated 15 chaotic stimuli from University of Chicago. Figure 9 shows a sample of four complex waveforms that we will be using to simulate our model. The stimuli range between negative and positive values; however, it's constrained within specific limits to avoid distorting the neuron. Excessively negative values can disrupt neuronal dynamics and lead to model failure.

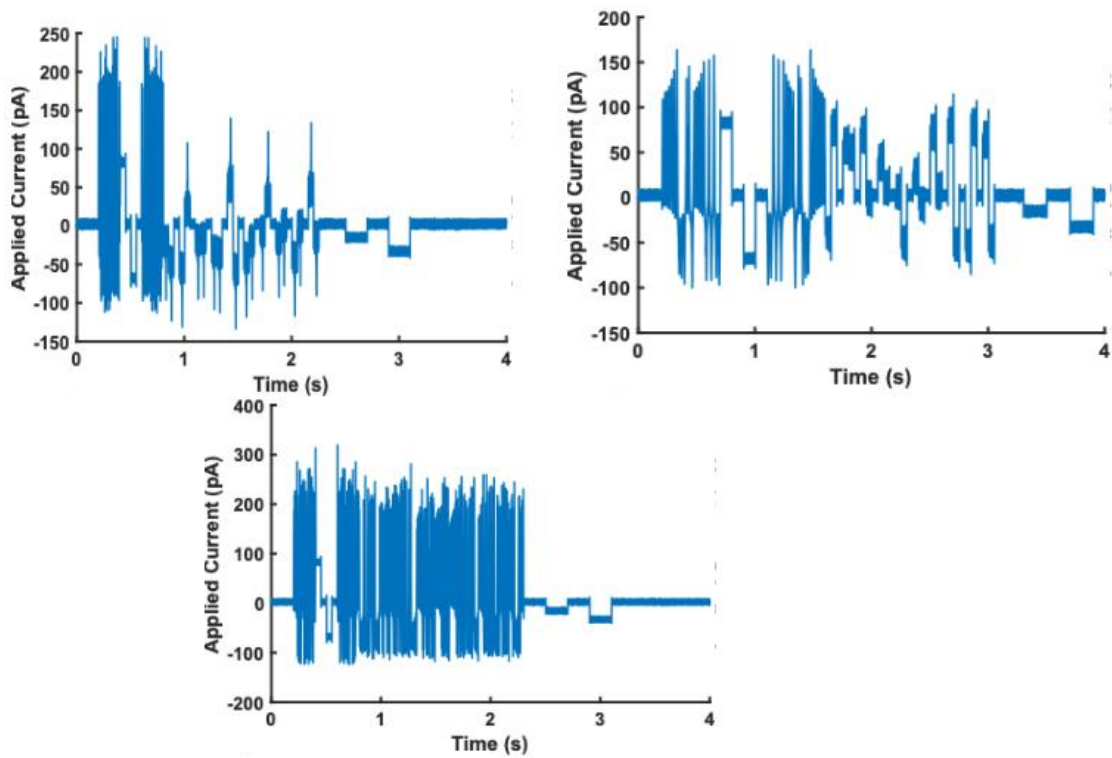


Figure 9: Different Waveforms of the Applied Pseudo-Noisy Current Presented to the Hvcx Model.

The pseudo noisy current has various waveform, time span, and frequencies as depicted in (a,b,c).

To better view the complexity of the stimuli, a zoomed version of three other stimuli is shown in Figure 10. This focused view allows for a clearer examination of the stimuli, facilitating a more detailed analysis of its influence on the neuronal responses.

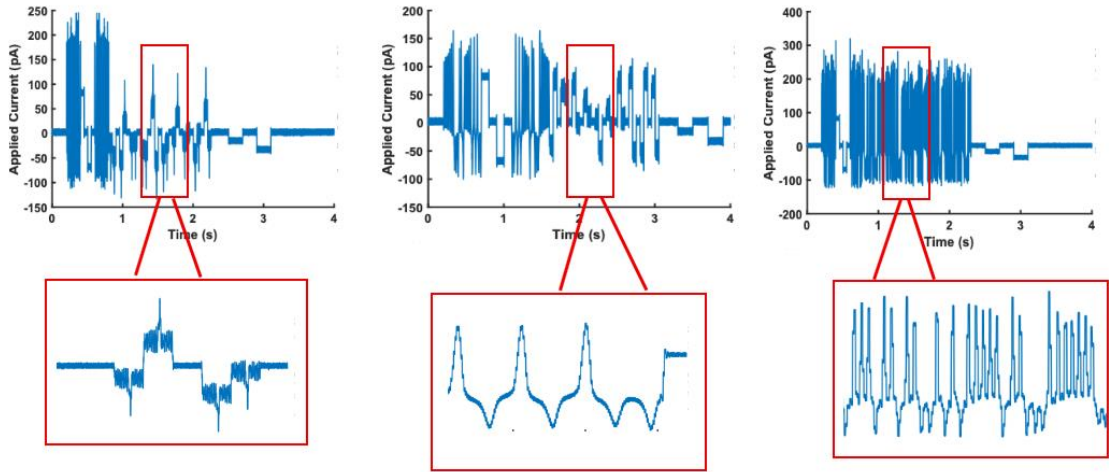


Figure 10: The Injected Stimulating Current  $I(t)$  Presented to the  $HVC_x$  Model.

Figure a, b, and c depict a detailed view of different intervals corresponding to various stimuli.

## D. Model Assessment

### 1. Features Extraction

To assess the goodness of our fit we developed a customized MATLAB code that extracts important features from the biological and model traces in response to the chaotic stimuli. The physiological features extracted from this function are spike timing, number of spikes, spike threshold, threshold voltage, spike amplitude, time to peak as shown in Figure 11.

The spike threshold was determined by isolating each spike and analyzing the rate of change of each signal ( $\frac{dV}{dT}$ ). The rate of change is computed for each element by taking the difference between the consecutive elements and dividing by a fixed time interval (0.1 ms, dictated by the sampling rate of the biological recording). If the calculated rate of change exceeds a predefined threshold of 10, the current element in the loop is identified as the threshold for the isolated spike. The time to peak is calculated as the time difference between the threshold time and the peak time of the spike. The time at which a spike occurred is extracted by a predefined function that is set to extract spikes on MATLAB.

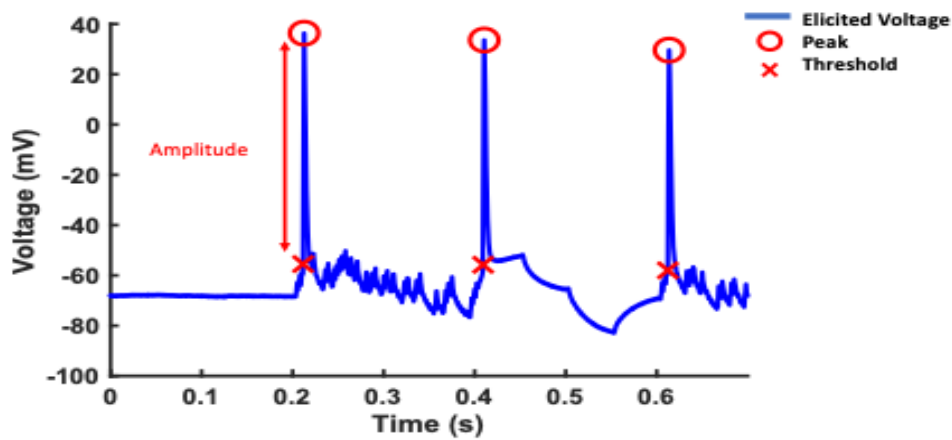


Figure 11: The Main Features Extracted from The Trace.

The feature includes the amplitude of the spike, the peak at which the spike occurs, threshold, time to peak, and spike width.

## 2. Comparing spikes

For enhanced visualization of the fitting results, we developed a new function that provides a comprehensive analysis of the spike accuracy and discrepancies between biological and model traces. After extracting the needed features from the spike, this function will allow us to analyze the features thoroughly by calculating the error between each feature in both traces.

We first extracted the spikes from each trace to analyze a spike per spike. We defined a fixed window before the spike with a value of (1 ms) and after the spike (2 ms) for each in both traces. This window is set to assure that the spike is extracted within a fixed window in both traces. Given the features extracted from the function before, we compare the extracted spikes morphology, timing, and threshold by adding a for loop that iterates over these detected spikes i.e., the iterations in the for loop are equal to maximum number of spikes between both traces. When looping over each spike in both spike trains

we calculate the errors in peak timing. The error is calculated based on the absolute difference spikes time in model trace and biological trace. We implement a logical condition checking whether the spike time error is less than 10 *ms*. If this condition is met, we consider this as a matched spike between the two traces and store its indices; otherwise, we label it as a missed spike (in either the biological or the model traces, respectively). We then proceed to calculate the errors associated with the morphology of the spike and threshold (see section 5). The function will also penalize the missed spikes and store their indices in a different array.

Thus, the function returns a vector of indices that indicate the timing at which the spikes were accurately fitted and another vector indicating the missed spikes for the model and biological trace respectively. It will also plot both traces and mark the missed and accurate spikes. Figure 12 illustrates the spike-marking and feature extraction procedure. First, spikes are detected independently using a predefined function that extracts all spikes in a spike train. The spikes times are used to align the biological and model traces. Spike occurring within a specified window  $\pm\Delta t$  are considered as matched spikes. These spikes are marked by red and blue circles and denoted as matched spikes in the biological and model traces, respectively. However, spikes present in the biological trace but lacking a corresponding model spike within the alignment window are labeled as missed events (black triangles), while additional model-generated spikes without biological counterparts are labeled as false events (green markers).

For each matched pair, we use the functions (See section 5) that will extract the spikes at their occurrence and calculate the least mean square error in morphology as: spike width, spike amplitude, threshold, time to peak, and spike timing. This approach

ensures that both firing pattern accuracy and spike-shape fidelity are simultaneously assessed.

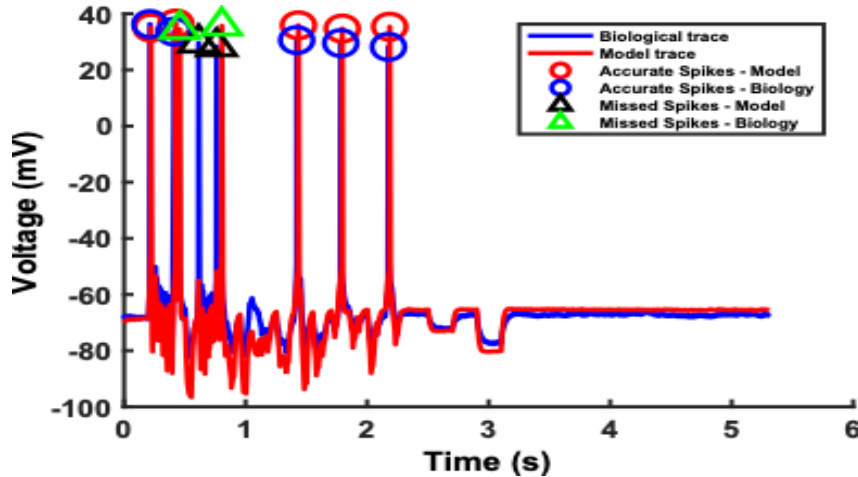


Figure 12: Overlay of Biological (Blue) And Hodgkin–Huxley Model-Simulated (Red) Voltage.

Overlay of biological (blue) and Hodgkin–Huxley model-simulated (red) voltage responses to identical stimulation. Illustrate the alignment used for spike detection and subsequent feature-extraction. The circular markers demonstrate spikes that match the timing exactly. Black triangular markers show spikes present in the biological trace but lacking a corresponding model spike within the alignment window. Green triangular markers are labeled for spikes generated by the model but miss their biological events.

### 3. *Parameter variations*

Once these functions are implemented, we add a for loop that iterates over the different values of the ionic channel conductance ( $g_{Na}$ ,  $g_K$ ,  $g_{SK}$ ,  $g_H$ ). For each iteration we store the conductance's values, feature's error, and spikes indices of the missed and overlaid spikes and present it in a separate text file as shown in table 2.

### 4. **Utilizing a New Error Metric**

Based on the above functions in MATLAB, we proceed to find the error in the spikes' features.

## 5. Spike Timing

For each spike timing at which the spikes are overlaid, we find the absolute difference between the timing of the biological trace and model.

Equation 49: Absolute Difference of Spike Time for Model and Biological Trace

$$e_i = |ST_b - ST_M|$$

Where  $i$  is the number of the specific spike and  $ST_b$  and  $ST_M$  are the spikes time for the biological trace and model traces respectively.

We then find the summation of the error for the whole spike train and average this by dividing by the number of the total number of non-missed pikes.

Equation 50: Averaged Spike Time Error

$$Total\ SpikesTime\ Error = \frac{\sum_i^n e_i}{n}$$

Where  $n$  is the number of non-missed spikes.

## 6. Error in Voltage Threshold:

To compute the threshold voltage error, we find the absolute difference between the corresponding threshold voltage of the biological trace and model trace.

We then find the summation of the error for the whole spike train and average this by dividing by the number of the total number of non-missed pikes as shown below.

Equation 51: Averaged Threshold Error

$$Total\ SpikesThreshold\ Error = \frac{\sum_i^n |Th_b - Th_M|}{n}$$

Where  $n$  is the number of the non-missed spike and  $i$  is the number of the corresponding spike in the spike train,  $Th_b$  and  $Th_M$  are the threshold voltage of the corresponding spike in the biological trace and model traces.

## 7. Error in spikes' width

For each action potential we find the spike width error by first detecting the half amplitude:

Equation 52: Half Amplitude

$$HalfAmplitude = ThresholdValue + \frac{(Amplitude)}{2}$$

The half-amplitude crossings were detected by searching for the last index-half-amplitude point before the spike peak and the first index-half-amplitude point after the peak. The temporal difference between these crossings was taken as the spike width.

Equation 53: Spike Width

$$Spike\ Width = abs(Left\ index - Right\ Index)$$

Equation 54: Averaged Spike Width Error

$$Total\ Spikes\ Width\ Error = \frac{\sum_i^n |SW_B - SW_M|}{n}$$

## 8. Error in Time to Peak

The error in time to peak is calculated by finding difference between the peak index the threshold index.

Equation 55: Time to Peak

$$Time\ to\ Peak = Peak\ Index - Threshold\ Index$$

Equation 56: Averaged Time to Peak Error

$$Total\ Time\ to\ Peak\ Error = \frac{\sum_i^n |TTP_B - TTP_M|}{n}$$

## 9. Using HPC cluster

To simulate our model, we used AUB High Performance Computers or HPC cluster which enables us to run our complex model more effectively The HPC consisted

of 880 cores and 3 TB memory which allow us to simulate many epochs at a shorter time. The code on HPC is parallelized and run in batches giving us the advantage of the coding being simulated faster than our personal computers. The access to HPC cluster was done through AUB IT which provided us with accounts and user ID. Once our simulation was done, we transferred all results as CSV files from HPC by using rsync command on SLURM.

## CHAPTER V

### RESULTS

Assessing neuronal fits based on the spike train alignment yields an inaccurate interpretation of the model's performance. Figure 13 illustrates a case where the spike timing of the simulated mode matches perfectly that of the biological recording. However, upon closer inspection at the level of the individual spike wave we notice significant discrepancies in the spike's morphology. This shows that even when spike timing is accurately captured, the model fails to replicate the true membrane dynamics, emphasizing the importance of assessing both spike timing and spike waveform characteristics when evaluating model performance.

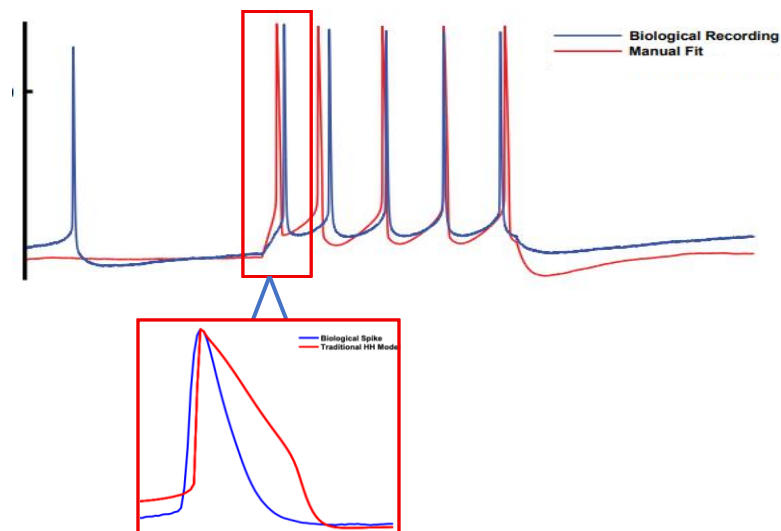


Figure 13: Biological and Model Trace Comparison.

A spike train showing matched number of spikes. The box under shows a closer look onto one spike that show discrepancies in the spike's morphology.

Therefore, in the first part of our work, we focused on adapting the classical Hodgkin–Huxley model to achieve a more realistic morphological representation of the biological voltage traces. Initial comparisons between the original model and the experimental recordings revealed clear discrepancies Figure 14. The classical model was unable to reproduce the characteristic shape of the biological spike, as shown from the deviation between the experimental trace in blue and the model output shown in black. The classical model generated action potentials with similar morphology across different neurons and input stimuli, leading to a poor representation of the biological neuron. A major source of this mismatch was the assumption of instantaneous activation, which generated gating transitions that were faster and more abrupt than those observed experimentally. As a result, the model produced an unrealistically steep rising phase and an inaccurate repolarization phase of the action potential.

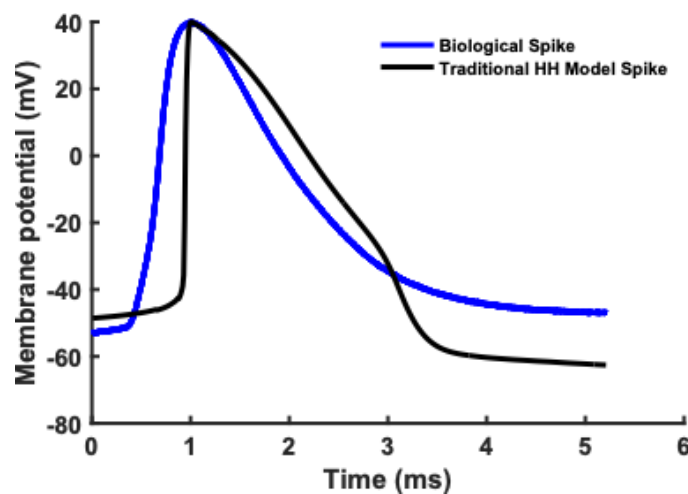


Figure 14: Comparison Between the Biological Spike (Blue) and the Classical Hodgkin–Huxley Model Spike (Black).

The classical model exhibits a sharper rise and broader repolarization phase, failing to capture the morphology and timing of the biological action potential.

Figure 14 illustrates that the original Hodgkin–Huxley model (black traces) produces an action potential with an unrealistically abrupt rise. This artifact emerges from assuming instantaneous sodium activation, which forces the channel to activate too quickly and distorts the overall spike shape compared to the biological recordings. To address this limitation, we reformulated the activation term as a time-dependent differential process and explored a wide parameter space for both activation and inactivation kinetics. Therefore, to better align the model and biological traces we re-parameterized the activation and inactivation kinetics of the sodium and potassium ion channels as mentioned earlier in the method section. Our first brute force explored a wide range of parameters that govern the activation and inactivation kinetics of the voltage-gated ion channels which directly influence the timing, steepness, and curvature of the action potential. The approach was adopted across a wide range of these parameters to avoid bias toward a local-optima and ensure a broad exploration of the non-linear parameter space. This step is particularly important in conductance – based models where small variation in gating kinetics can lead to large discrepancies in spike morphology. Our results show, varying the parameters that governed the steady-state activation and inactivation of the ion channels, along with time constants led to clear changes in the shape of the modeled action potential. The brute force search revealed that the model is strongly governed by the chosen parameters as reflected by the wide spread of the MSE values across the different parameter combination. This spread reflects the high sensitivity of the nonlinear model to these empirical parameters reflecting the non-trivial relation between the model behavior and the parameters. To better illustrate this, we first present the results for  $HVC_x^1$  by comparing 5 poor fits with highest MSE values with other 5 decent fits with lowest MSE as shown in Figure 15. The black fits show clear

deviation from the biological trace (blue) in terms of threshold, voltage onset, steepness of the rising phase and repolarization phase. However, the red traces closely overlay the biological trace by matching the different features of the spike. We also notice from all figures using the differential form of the  $m$  activation gating variable introduces a time dependent dynamic which smoothens the voltage transition and shapes the action potential well.

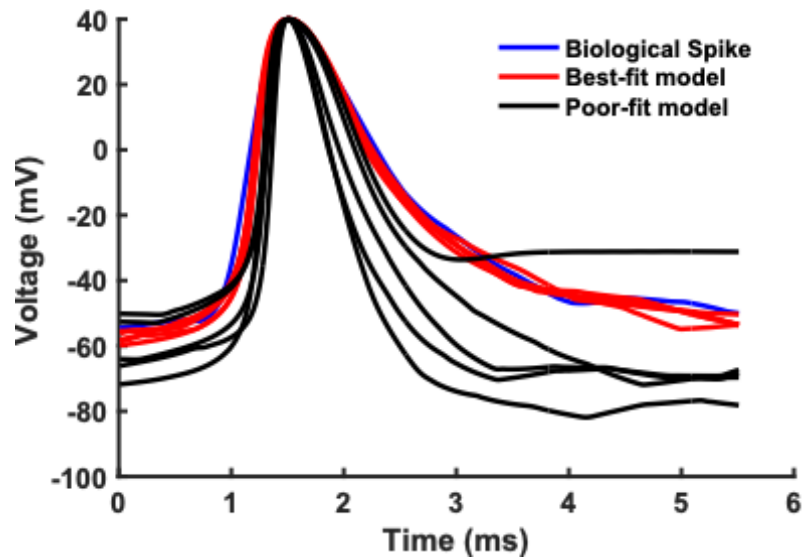


Figure 15: Comparison Between Biological Voltage Traces and Model Simulations.

The five best-fitting models are shown in red, while poorly fitted models are shown for contrast.

The same analysis was applied on other neurons to assess the consistency of our analysis. These neurons consisted of three  $HVC_x$  neurons that were stimulated by a step current and another with a chaotic current. We observed that the overall morphology of the action potential was predominantly uniform across all neurons analyzed in the traditional model. The rising phase exhibited a steep action potential upstroke with a fast, nearly linear repolarization phase reflecting the instantaneous dynamics of the gating

variable in the classical model. Figure 16 shows the black curve which exhibits clear discrepancies from the biological trace in the four neurons. However, the conducted brute force search for the 4 neurons also revealed a large spread of the MSE values across the different iterations. Thus, we chose parameter combinations with the lowest MSE value and plotted them. We notice that the agreement between the modeled and biological spike traces significantly improved when the channel kinetics were changed. The red traces across the different neurons reflect substantial improvement in the agreement between and biological spike shapes in terms of the upstroke and the repolarization phase.

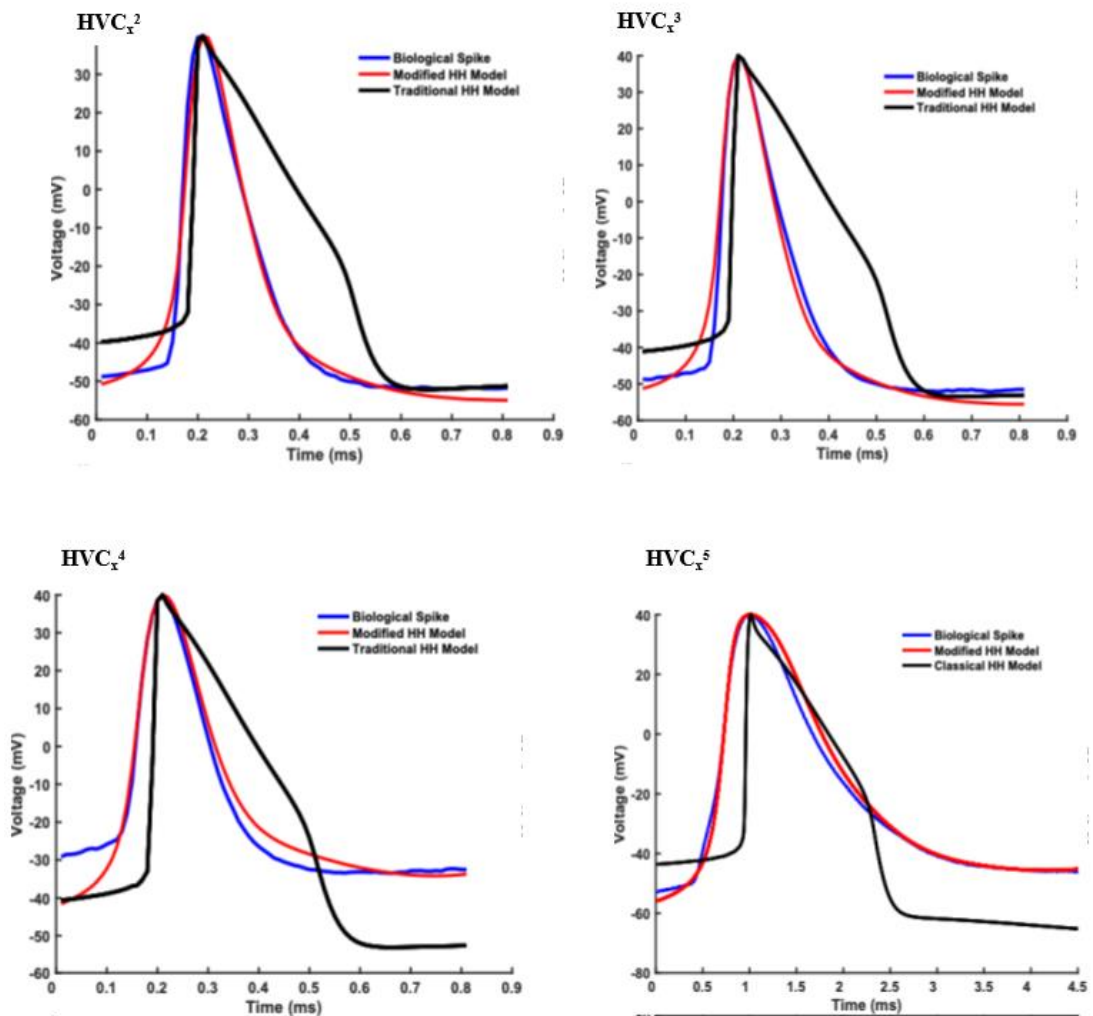


Figure 16. Brute Force Search Results for Optimal Parameters for Each Neuron

Overlay of biological voltage traces with model simulations. The five best-fitting models are shown in red, while poorly fitted models are included for comparison.

After obtaining a satisfactory fit for an individual action potential, we fixed the corresponding parameter set for each neuron and subsequently adjusted the maximal conductance through a brute force search to find a decent fit for the whole spike train. Figure 17 shows the three decent fits obtained for  $HVC_x^2$ ,  $HVC_x^3$ , and  $HVC_x^4$  where the model now matches the spike morphology and spike timing in addition to the number of spikes.

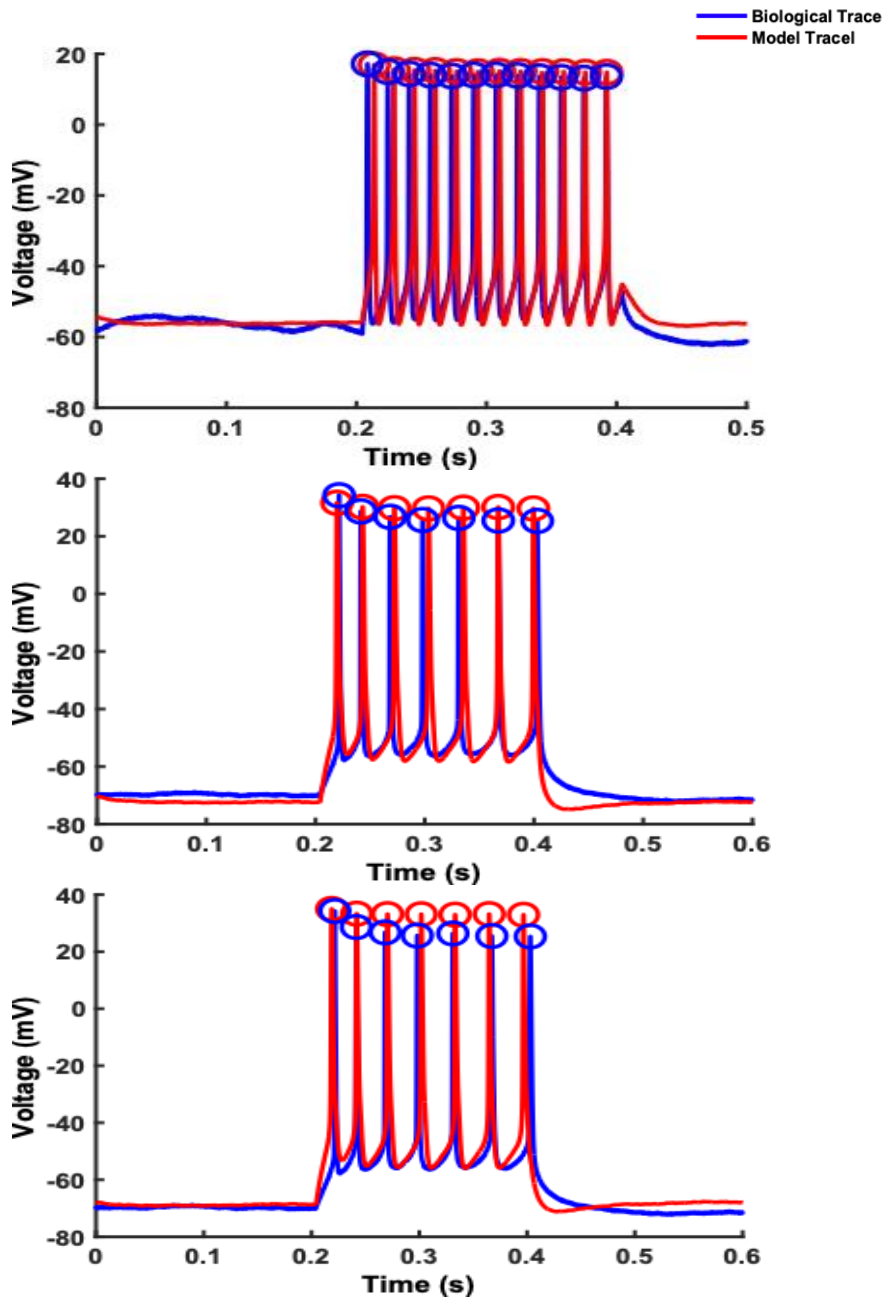


Figure 17: Model Closely Matches Biological Spike Timing and Shape

Overlay of biological (blue) and model (red) traces for three HVC<sub>x</sub> neurons, showing close agreement in spike timing and morphology.

In the next part of our work, we focused on optimizing the neuronal model fits simulated by a pseudo noisy stimulus. In this section we investigate the fitting performance of the model using a chaotic stimulus. We had a large data set of chaotic stimuli from UC Chicago with the biological neuron response. Figure 18 show a sample

of the biological response corresponding to different stimuli given to the same neuron. Unlike step currents, neurons simulated with a chaotic input, produce a response that appears irregular and less structured compared to the clean spike trains elicited by step currents.

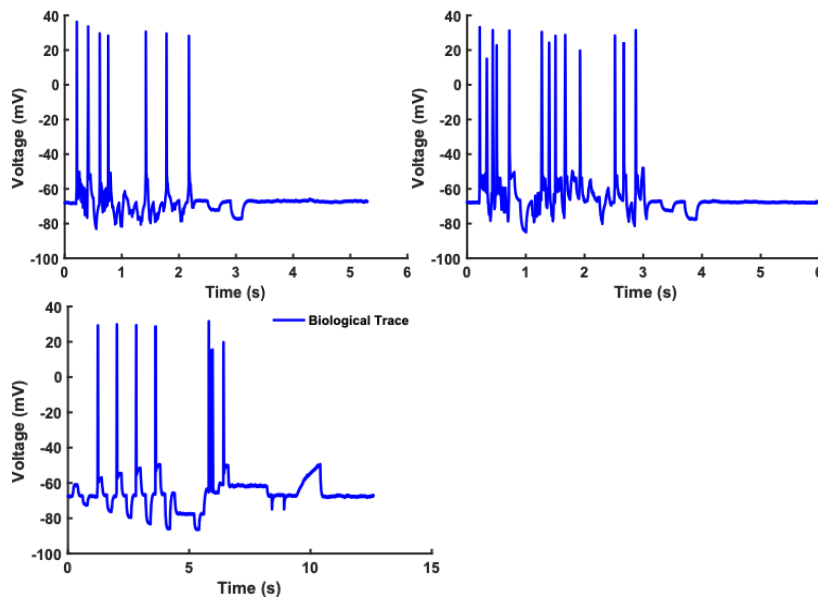


Figure 18: Sample of Three Biological Recordings

The three plots show a sample of the biological recordings illustrating the shape of the voltage traces when stimulated by a chaotic stimulus.

To optimize the neuronal model fits, we performed a brute-force parameter exploration as mentioned in the methods section and evaluated each candidate model using our customized MATLAB function to determine which parameter set reproduced the biological data correctly. Optimal parameter sets are those capable of accurately reproducing essential electrophysiological characteristics of the neuron, including the total spike count, the detailed shape of individual spikes, and the precise timing of spike events. These features serve as the foundation for evaluating how faithfully the model

reflects the biophysical behavior of the recorded neuron. For the same neuron, multiple current-clamp stimuli were tested to examine the robustness of the parameter sets and stimuli. In Figure 19 we show different epochs along with their biological response. Our findings revealed that a single parameter configuration did not consistently yield the correct spike count across all stimuli. Specifically, for HVC<sub>x</sub><sup>1</sup>, only Epoch 7 out of the 15 applied stimuli produced the correct number of spikes. This highlights the stimulus-dependent nature of neuronal dynamics and underscores the difficulty of identifying parameter sets that generalize reliably across varying input conditions.

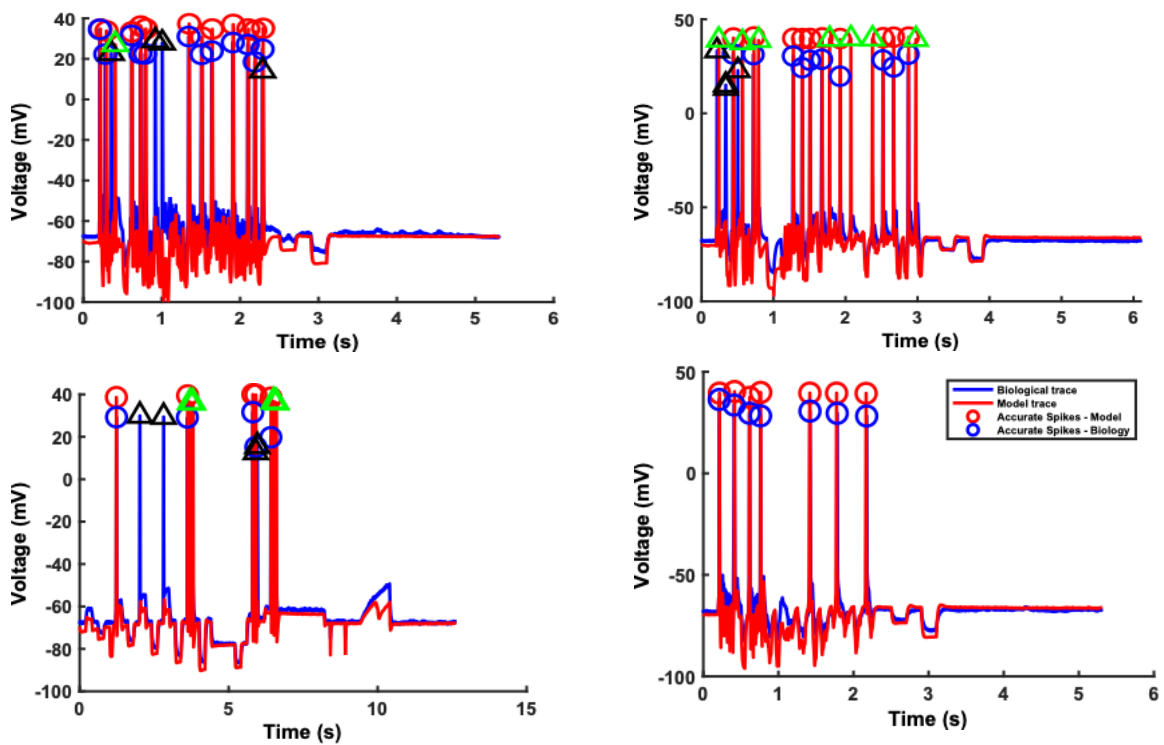


Figure 19: Model and Biological Spike Trains Aligned Across Epochs

Overlay of biological (blue) and model (red) spike trains with peak markers. The panels show different epochs applied to the same neuron and their corresponding biological response along with the model simulation overlaid.

Once we identified a neuron–stimulus pair that produced the correct number of spikes, we proceeded with the analysis by examining the spike morphology in detail. For each spike, we extracted a set of quantitative features from both the biological trace and the corresponding model output. These features—including spike time, spike count, amplitude, threshold voltage and timing, and time to peak—are essential for evaluating model performance. For each parameter run, we calculated the different errors for each feature between the model and biological trace, least mean square error for each extracted spike in term of the morphology of the spike. These features are important in terms of assessing the discrepancies in the shape of each spike and the overall shape of the spike train. To carry out the optimization process we performed objective optimization where the objective represents the extracted feature to be minimized. The optimization process focuses on minimizing two independent error metrics simultaneously to identify parameter combinations that produce the best overall fit. Analyzing the relationship between these error metrics allow us to explore whether a global minimum exists in a two-dimensional parameter space. Figure 20 summarize the behavior of these errors and shows the tradeoffs between the different error metrics. In these plots, each point corresponds to the averaged error of a model, and the clustering of points shows that multiple parameters set yield very similar error values. For example, in Figure 20A, we plotted the averaged amplitude error against the averaged threshold error to identify regions in which both metrics are minimized. Both errors exhibited their lowest values at closely similar  $g_{Na}$  levels. Beyond this region, altering the conductance parameters led to a simultaneous increase in both error measures. However, in an opposite relation is shown between the averaged spike width error and the averaged amplitude error. For a parameter set that gives us the highest amplitude error the spike width error is at it

minimum and vice versa. Figure 20 C,D , and E illustrate a similar trade-off between the described error metrics. Figure F shows a positive relationship between time-to-peak error and spike-width error, indicating that both features are minimized in the same region of parameter space.

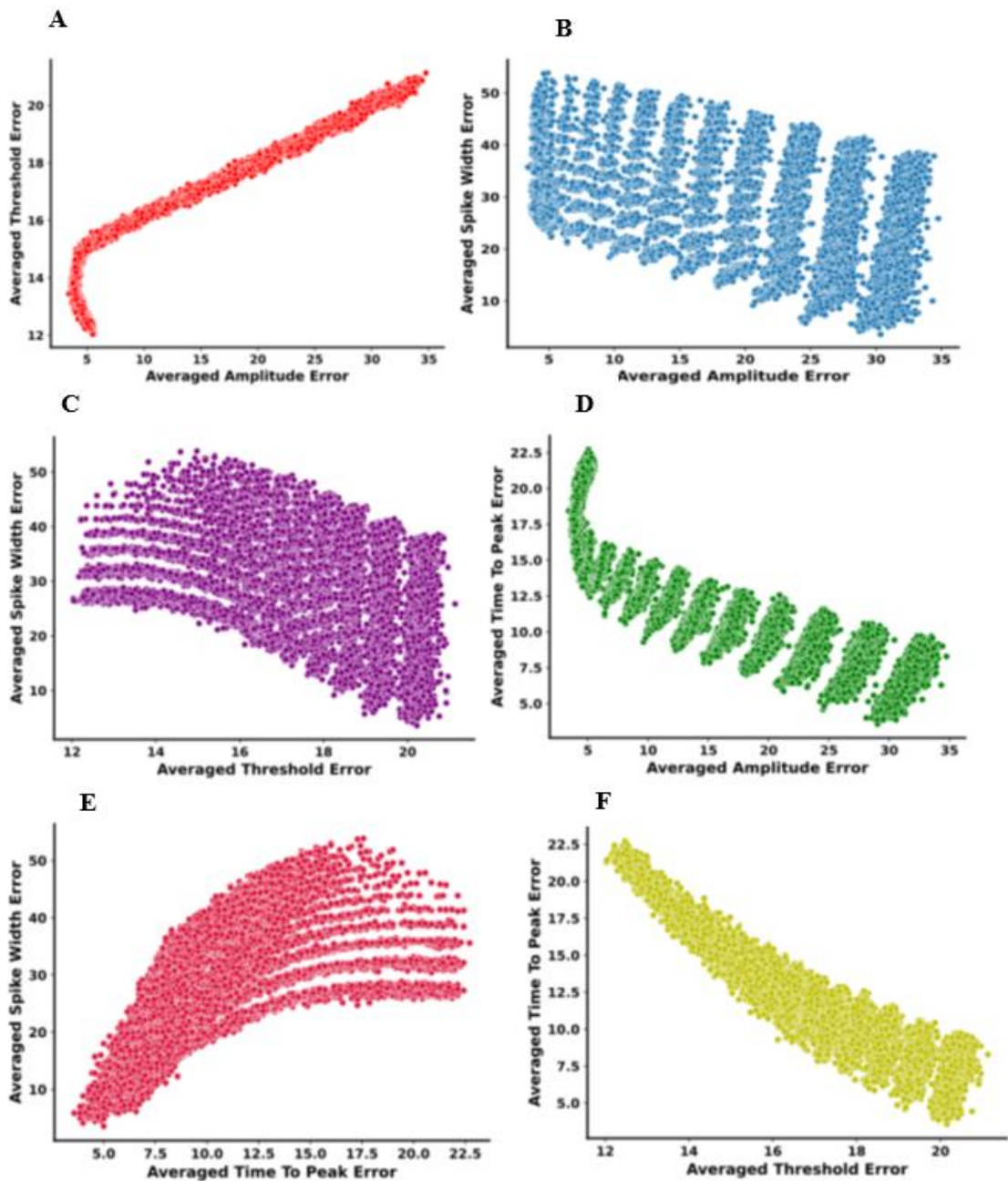


Figure 20: Feature-Feature Trade-Off Plots

The plots show relationships between pairs of error metrics across the explored parameter space. Each point represents a model parameter set, illustrating competing objectives and the absence of a single global minimum.

To better interpret this relationship, we selected several points from each plot and overlaid their corresponding model-generated spikes onto the biological spike. The traces shown in Figures 21 different colors reveal how different parameter sets affect spike. Figure 21A illustrates the relationship between amplitude error and threshold error. At this conductance value, the model's threshold curve (red) aligns most closely with the biological data (blue), and the amplitude error likewise reaches its lowest value Figure 21A. The other points extracted from the plot show higher error values where the threshold and amplitude error deviate from the biological spike as shown in the black and pink curves.

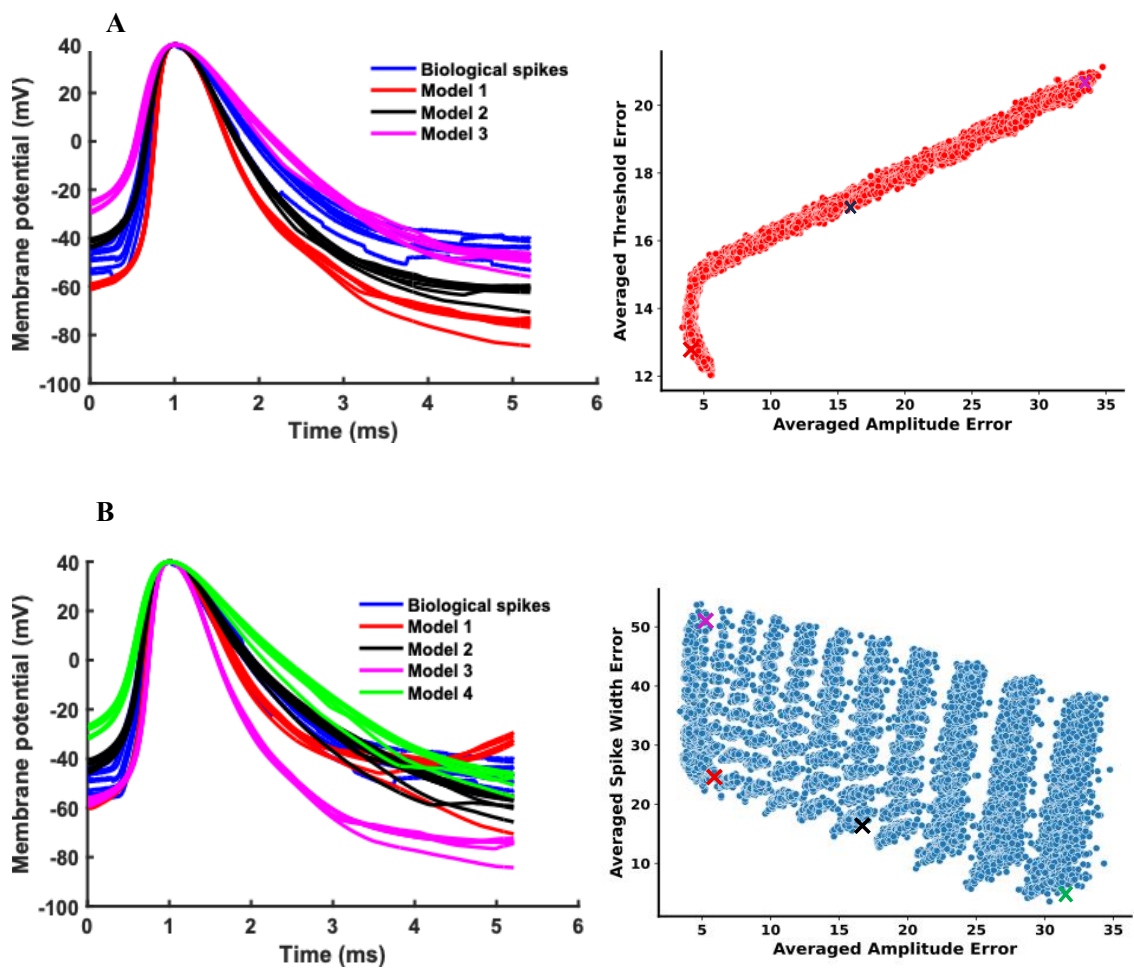
We performed a similar comparison for the remaining extracted features. In Figure 21B, we selected four representative points to assess whether a trade-off exists between spike width error and amplitude error. The point with the minimum combined error, shown in black, demonstrates a close agreement between the model and biological spike width as well as amplitude.

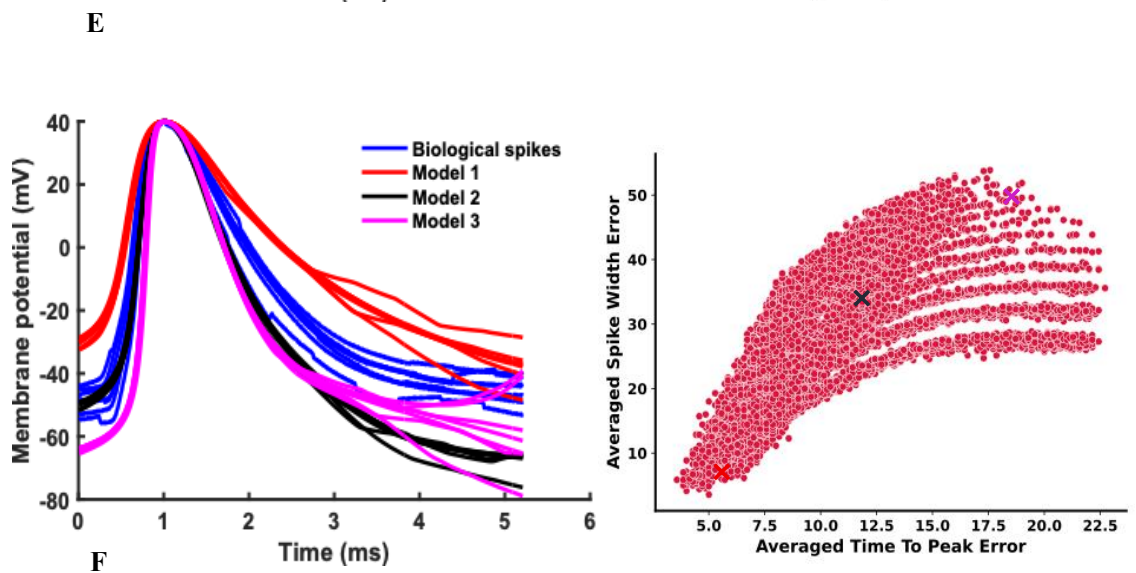
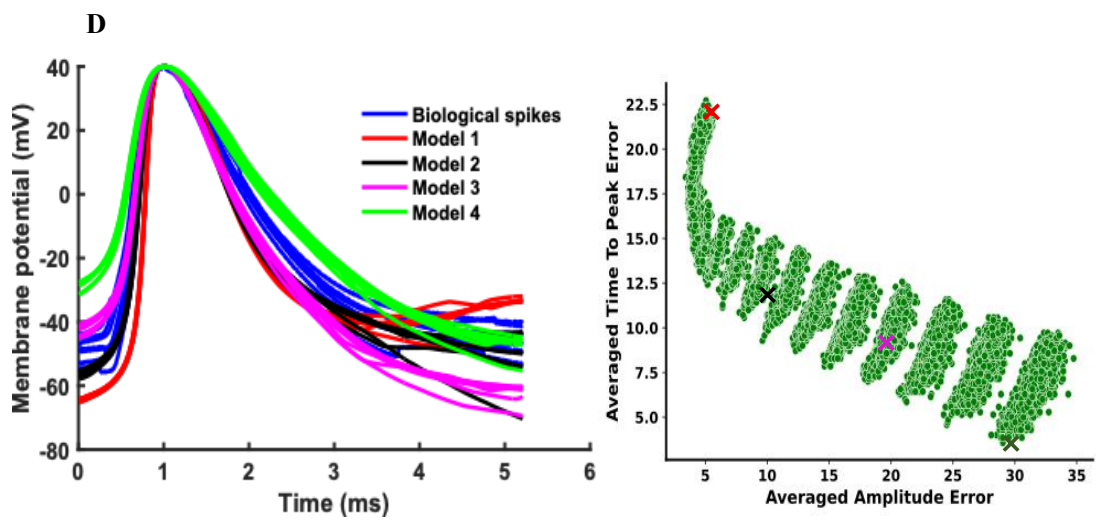
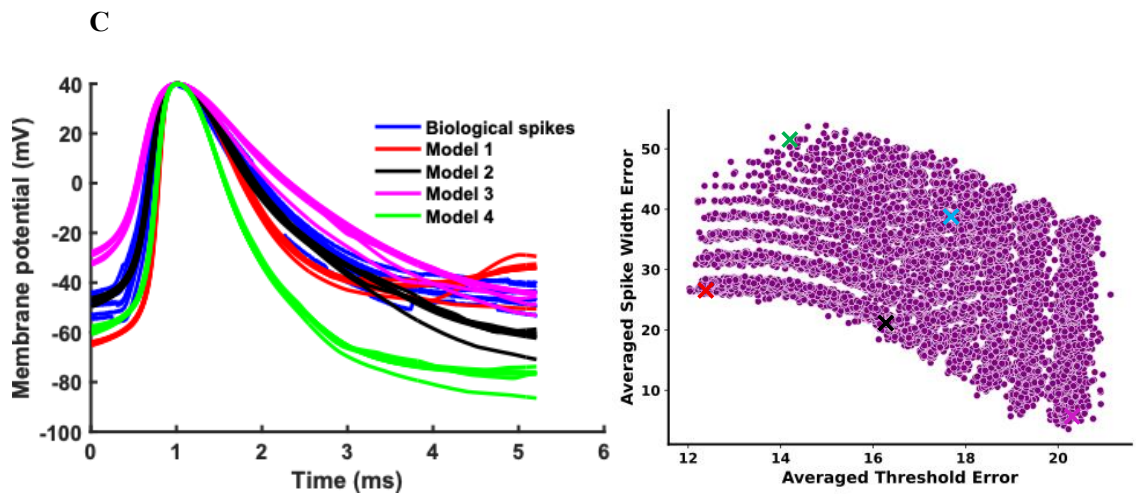
In Figure 21C we depict a similar relation between the averaged threshold error and spike width error. The four representative points shown in the plots in the left show that the threshold error has lowest value at higher spike width error as revealed in the red trace (minimum threshold error ) while the lowest spike width occurs at a higher threshold error.

Figure 21D illustrates the relationship between amplitude error and time-to-peak error. A different relationship emerges between amplitude and time-to-peak errors:

reducing the amplitude error often comes at the expense of increasing the time-to-peak error. This is evident in the left plot where the red trace shows a longer time to reach the peak while the amplitude error is minimum. Figure 21E shows a positive relation between the time to peak and spike width error. The red trace shows the lowest time to reach the spike with a minimum point error at this point.

Figure 21F show a negative relation between the threshold and time to peak error.





**F**

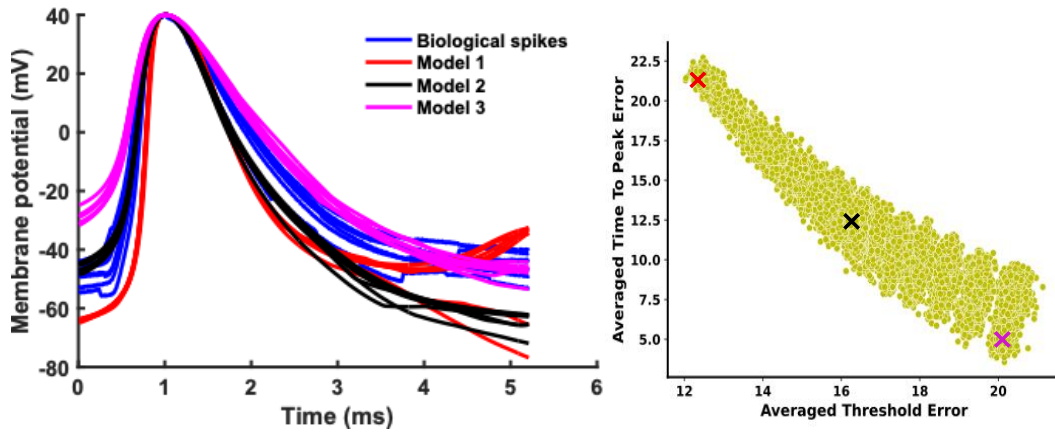
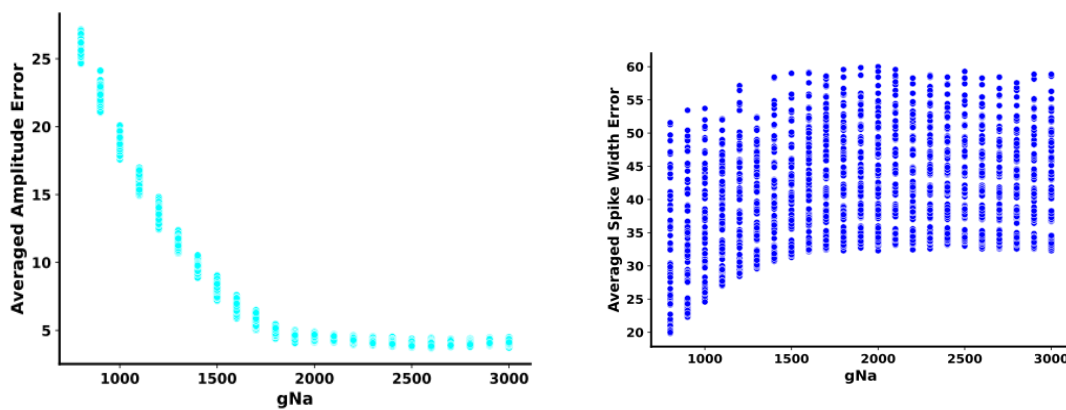


Figure 21: Spike Overlays and Feature-Error Trade-Offs Across Parameters

Overlay of biological and model spikes (left) and feature-error relationships (right), showing how amplitude, time-to-peak, spike-width errors, and threshold vary across parameter sets.

We also examined the relation of the different error metrics with respect to the varying conductance's. Figure 22 show spike width error, amplitude error, threshold error, and time to peak vary with respect to the  $g_{Na}$  values. It is evident from the plots that the amplitude error, threshold error, and time-to-peak error are primarily influenced by changes in the rising phase controlled by  $g_{Na}$ .



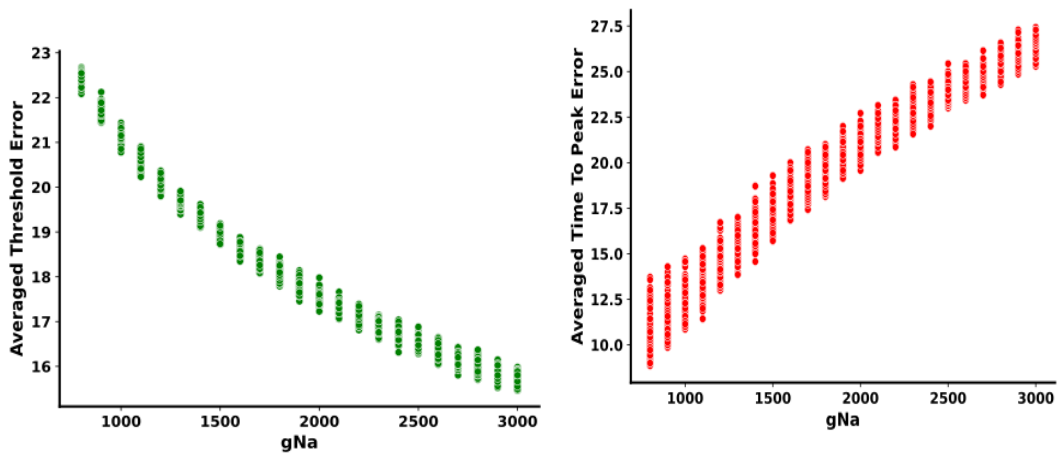


Figure 22: Averaged Feature-Specific Errors as a Function of Sodium Conductance

Each panel shows how a different spike feature—amplitude, spike width, threshold, and time-to-peak—varies across the tested  $g_{Na}$  values.

Similarly, we examined the relation between the  $g_K$  conductance's and the different error metrics as shown in Figure 23. We notice only the spike width error is predominantly affected by changes in  $g_K$ , indicating that potassium conductance primarily governs the repolarization phase and overall spike duration as well as the spike width.

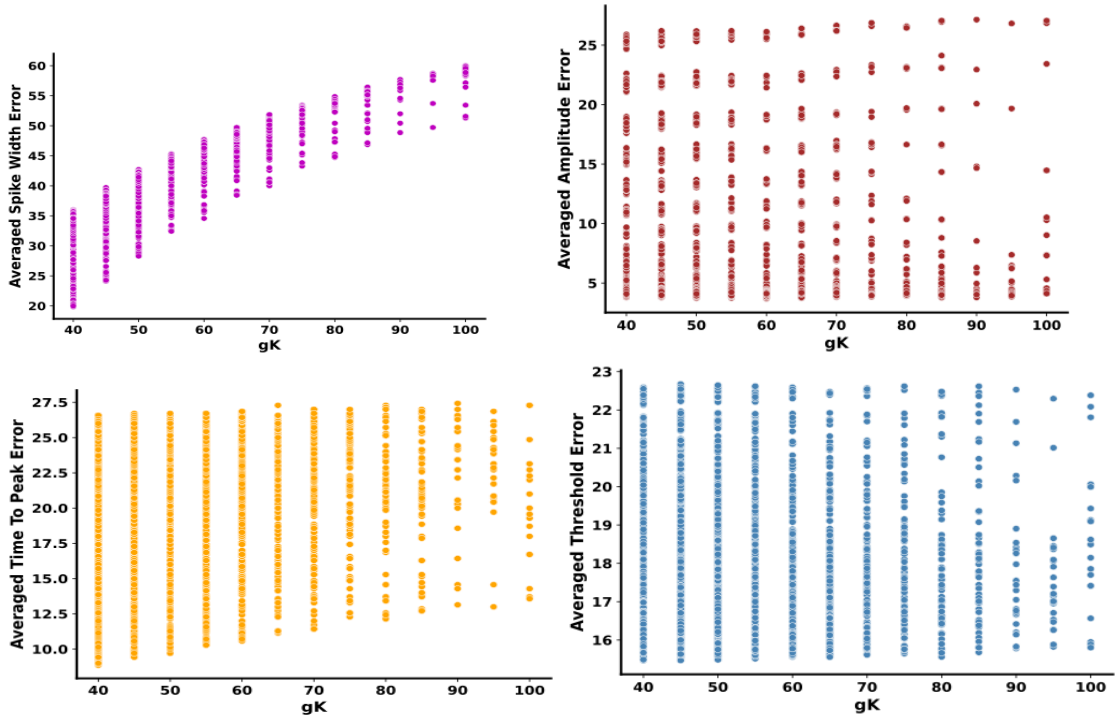


Figure 23: Averaged Feature-Specific Errors as a Function of Potassium Conductance.

Each panel shows how a different spike feature—amplitude, spike width, threshold, and time-to-peak—varies across the tested gK values.

In Figure 24, we plotted the distribution of the optimized parameters for the different activation and inactivation variables corresponding to the ionic channels. The boxplots show the parameter ( $k_{2m} - k_{6h}$ ) for each of the neurons  $HVC_{x1}$  through  $HVC_{x5}$  corresponding to the gating variable  $m$  that control the upstroke of the action potential. The colored markers denote the optimal parameter values obtained for each individual neuron, whereas the black marker represents the classical Hodgkin–Huxley parameter. We observe that several optimized parameters deviate noticeably from their classical Hodgkin–Huxley values, particularly  $k_{2m}$ ,  $k_{4m}$ ,  $k_{5h}$ ,  $k_{6h}$ , and  $k_{7h}$ . In contrast,  $k_{3m}$  remains close to the standard value in most neurons, with clear deviations appearing only in  $HVC_{x3}$  and  $HVC_{x5}$ .

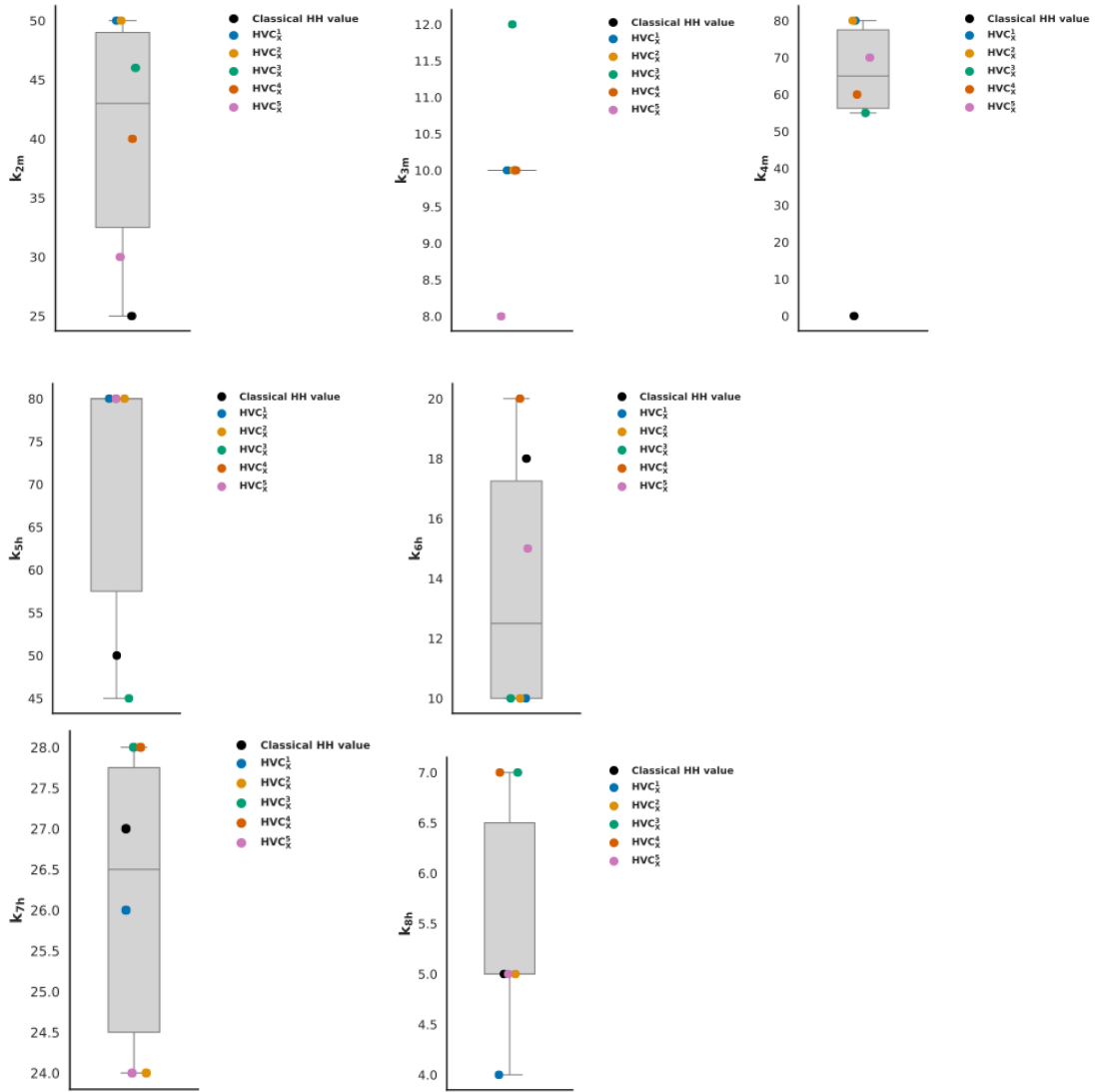


Figure 24: Boxplots Showing the Distribution of Optimized Model Parameters across Neurons.

In each panel, the box represents the interquartile range, the central line indicates the median, whiskers show the spread of values, colored markers denote neuron-specific

Similarly, we did the same for the parameters corresponding to the activation kinetics of the potassium channels as illustrated in Figure 25. These parameters regulate the shape of the downstroke of the action potential. We observe that several optimized parameters deviate noticeably from their classical Hodgkin–Huxley values, particularly  $k_{10n}$ ,  $k_{11n}$ ,  $k_{12n}$ , and  $k_{13n}$ . In contrast,  $k_{9n}$  remains close to the standard value in most neurons, with clear deviations appearing only in  $HVC_x^1$ ,  $HVC_x^2$ , and  $HVC_x^3$ .

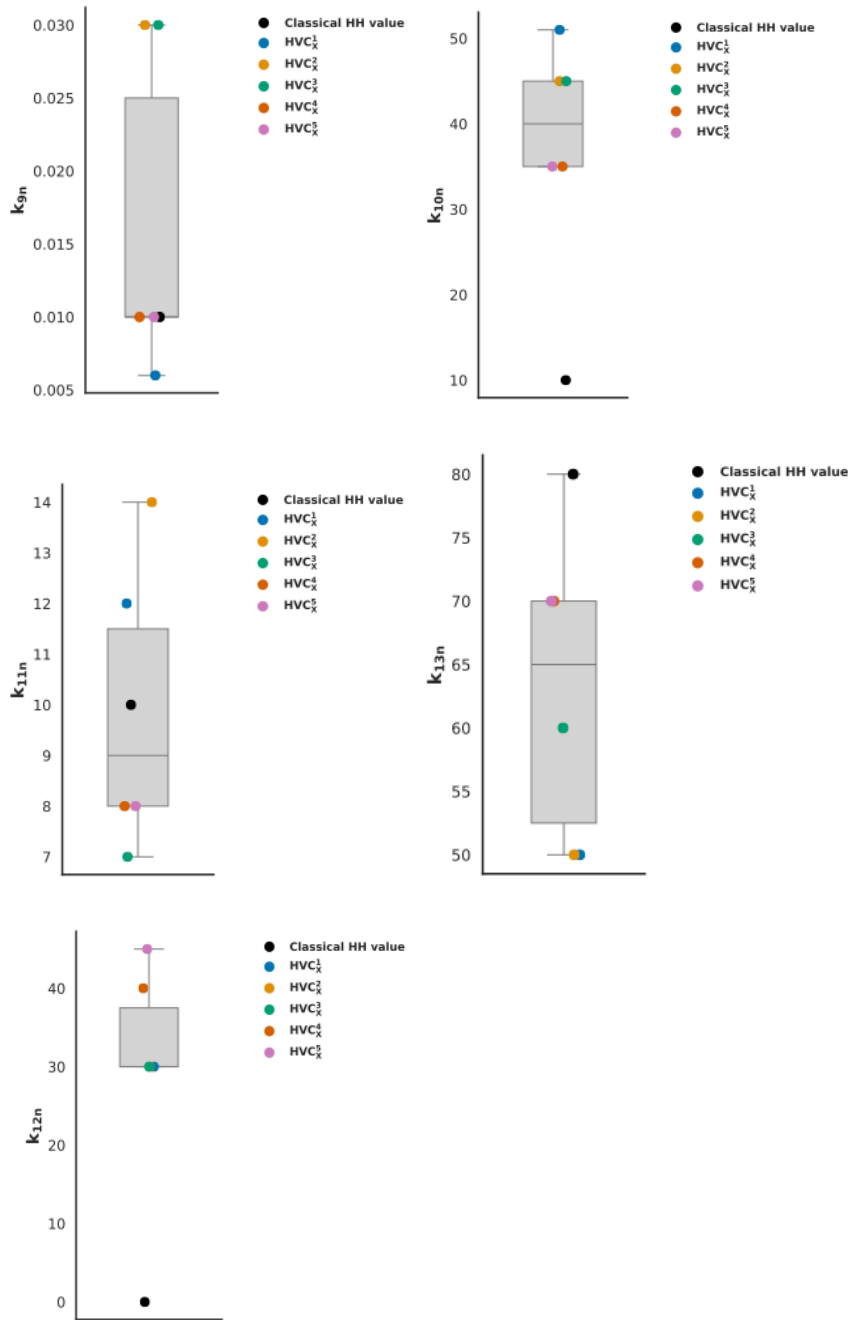


Figure 25: Boxplots Showing the Distribution of Optimized Model Parameters across Neurons

In each panel, the box represents the interquartile range, the central line indicates the median, whiskers show the spread of values, colored markers denote neuron-specific optimized parameters, and the black marker indicates the classical Hodgkin–Huxley value.

After completing the optimization process, we inspected the fitted parameters and their effectiveness in capturing key spike features. We then applied the parameter sets yielding minimum errors to the model to obtain a good fit under the pseudo-noisy stimulus. We applied a wide range parameter search of the maximal conductance ( $g_{Na}$ ,  $g_H$ , and  $g_{SK}$ ) through HPC. Based on the feature-feature plots we examined the models performance and chose parameters that can give a decent fit.

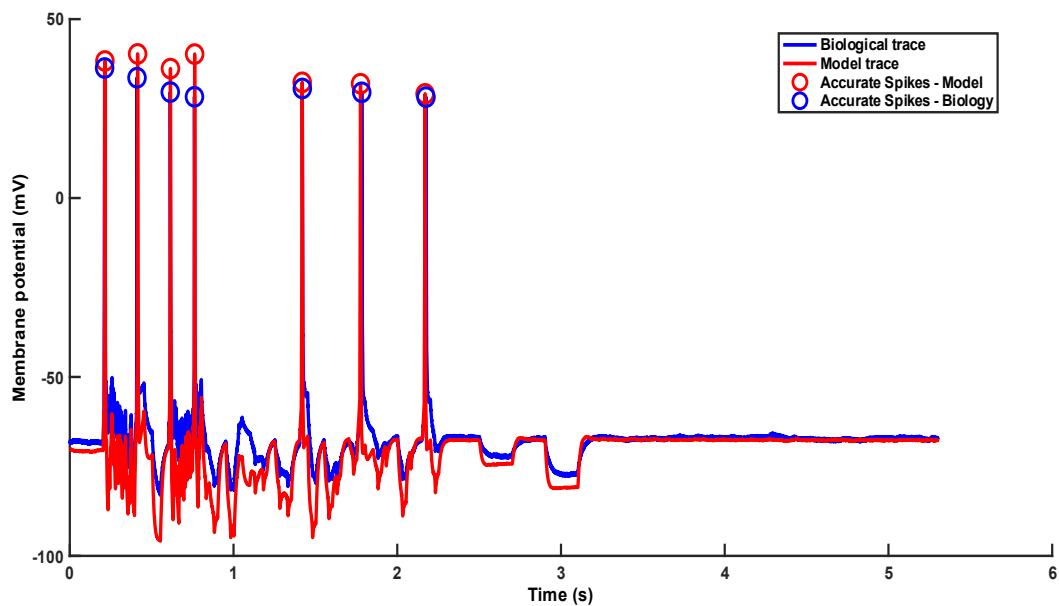


Figure 26: A Final Optimized Plot Showing the Model and Biological Traces Overlaid  
The model traces matches the exact number of spikes of the biological trace

## CHAPTER VI

### DISCUSSION

In this study, we aimed in improving quantitative fitting of the conductance-based models to experimental recordings. From a biological perspective, a spike embraces more information than its specific timing only; its intrinsic properties are reflected in the morphology of the spike. While the traditional HH model can replicate the spike timing, a closer inspection reveals large discrepancies in spike shape and underlying dynamics. Spike times are therefore insufficient to resemble the fidelity of the model. Our work aims in optimizing the neuronal model fits allowing a faithful replication of the model. The shape of the action potential is controlled by interaction between different ionic channels which are governed by differential equations and specific parameters. Therefore, instead of focusing only on spikes times, we targeted the shape of the action potential by tuning the parameters of the underlying differential equations. In our work we tackled the activation kinetics of the main channels: sodium and potassium. These channels consist of gating variables that control the opening and closing of their channels. Each gating variable is governed by differential equations that model their behavior.

We further examine the effect of the stimulus on fitting neuronal model. We utilized a pseudo-noisy stimulus and explored different regimes of the parameter space that can produce decent fits. We noticed a single neuron stimulated by different chaotic stimuli lead to different performance in which not all resulted in good fits. While individualized customization of the Hodgkin–Huxley model yielded better fits in spike morphology, precise reproduction of spike timing was primarily influenced by the type of stimulus applied.

Moreover, for each neuron and stimulation condition (chaotic or step current), we ran a brute-force search across parameter space, using high-performance computing to test many model configurations. Through customized MATLAB functions we analyzed the performance of the model. Each candidate model was evaluated using feature-based error measures that account for both spike timing and spike shape.

Our results demonstrate that relying on empirical parameters from experimental results had shown to produce inaccurate spikes' morphology despite matching spikes time.

Our results suggest that no universal conductance-based model can faithfully capture the highly nonlinear dynamics of all neurons; each neuron required its own tailored set of parameters. For simplicity, traditional HH models deal with the  $m$  gating variable to evolve instantaneously, assuming that sodium channels activate rapidly and thus reach their equilibrium states almost immediately (([Song et al.,2009](#))). Although this assumption simplifies the model, it consistently causes a steep rise in the depolarization phase of the action potential. The steep rise is revealed in our simulations shown in Figure 14 where the traditional HH model shows a sharp rise in the depolarization phase across the different neurons. The  $m$  gating variable describes the opening of the sodium channels, where the rate of this opening is controlled by rate constant  $\alpha$ . When dealing with assumption the model neglects the true biophysical reaction occurring and thus mismatches the biological recording. Upon updating the formula, we notice a smooth increase in the depolarization phase demonstrated in Figure 15.

Moreover, traditional HH models use empirical parameters taken from experimental recordings and are widely used as universal parameters when modeling different neurons. Our results show that no set of parameters can be applied to all neurons.

For every neuron, we explored a large range of parameters that are directly responsible for the gating variable governing the shape of the action potential. Through this exploration, we found that many different parameter sets can generate comparable firing behavior, yet only a fraction of them reproduce the detailed shape of the action potential. This allowed us to identify parameter sets that are unique for each neuron and capable of reproducing the biological recording to a very high accuracy. This sheds light on why models relying on standard and fixed parameter values tend to produce uniform spike morphologies as shown in the classical HH model in Figure 16 although the governing equations allow diverse dynamics, using fixed empirical parameters confine the model to a limited operating range. By loosening these parameter constraints and expanding our search across the parameter space, we obtained a wider spectrum of spike shapes that more closely match experimental recordings. This is very significant when dealing with highly nonlinear models where a minor variation in parameter values can produce substantial change in the model's output. Our results demonstrate a significant improvement in the spike's morphology once we found the appropriate parameters. The curve matches well the spike features: latency of the first spike, threshold, amplitude, width, after hyperpolarization. These features are essential due to their biological relevance. Classical HH models usually tend to produce stereotyped spikes as shown in our simulations however spikes are not alike in all neurons. Action potential morphology is not uniform across the brain but instead reflects the specific ion channel composition and structural properties of each neuron, which together shape all phases of the spike from its rapid depolarization to the post-spike membrane dynamics. The shape of the action potential is unique to the neuron's biological role. For instance, neurons that release neuromodulators tend to have broader spikes that support sustained calcium entry,

whereas inhibitory and fast-spiking neurons generate narrow spikes optimized for high-frequency firing (Bean et al., 2007). Therefore, given the fact the spike waveform plays a key role in neuronal signaling and synaptic transmission, capturing action potential morphology when using neuronal models is necessary to produce meaningful neuron models. In Figure 17 we applied the optimized parameters to simulate spike trains. Upon, customizing the model to new parameters that match the spike we were able to produce decent fits. The simulations show that both spike timing and spike shape closely match the biological recordings for the neurons studied.

In the next part of our work, we used a pseudo-noisy stimulus to investigate how different stimulus types influence the fitting performance of the model. Unlike step currents, which often evoke regular and stereotyped firing patterns, chaotic stimuli continuously perturb the membrane potential and generate highly irregular spike trains. The chaotic stimuli allowed us to investigate how the model responds to continuously varying inputs and to reveal important mechanisms underlying the interaction between external stimuli and neuronal dynamics. A single neuron was stimulated by different stimuli under which each elicited a different voltage response as shown in Figure 19. Despite good agreement in spike shape (Figure 18), precise alignment of spike timing was more difficult to achieve. Only 1 epoch of the 15 epochs was able to generate a spike with exact timing. Stimulating the same neuron with different chaotic inputs leads to variable model performance, as not all stimuli yield equally accurate fits. A model optimized under one chaotic stimulus may reproduce neuronal behavior only within the specific dynamical regime explored by that input. Other chaotic waveforms, characterized by distinct amplitude distributions, frequency content, or temporal structures, can drive the neuron through different voltage ranges and gating-variable states. If the model

parameters do not faithfully capture the underlying ion-channel dynamics, model performance fails when exposed to these new dynamical regimes. In addition, the way a chaotic current stimulates the neuron differ from one to another due to the ionic channels each activate. This explains why certain stimuli result in accurate spike timing and morphology, while others do not.

Figure 18 show a significant alignment of the model's spike morphology to the biological recording which in turns support our model. This provides a more stringent test of model performance to find the optimal parameter sets that accurately capture the intrinsic neuronal dynamics that can capture spike morphology under such complex input conditions.

The pseudo-noise stimuli generated good fits to biological data once we optimized the activation and inactivation kinetics of the gating variables and under the appropriate stimulus. The parameters that generate the minimum errors varied from one stimulus to another, hinting that model parameters' choice and optimization is also stimulus dependent. While different stimuli explore different regimes in the dynamical system, all of them intersect at key parameters that are fundamental for the model neuron's behavior. In particular, the half-activation and half-inactivation parameters for the  $\text{Na}^+$  current, as well as the slope of the  $\text{K}^+$  current's activation govern the upstrokes and downstrokes of action potentials almost solely independent of all ionic currents incorporated. Moreover, the  $\text{Ca}^{2+}$ -dependent  $\text{K}^+$  conductance modulates the frequency of firing and the spike timing.

The fitting process allowed us to assess the variability in intrinsic neuronal properties across neurons. In addition to the fact the neuron's error metrics strongly demonstrate variability once we changed the maximal parameters. It also provides a

framework to explore regions of parameter space where feature-specific error minima occur and to examine trade-offs between different electrophysiological features. The feature space exploration highlighted multiple islands of parameters that share common local minima, hinting to the homeostatic mechanisms that biological neurons undergo where multiple combinations of intrinsic properties can generate the same firing pattern. The different relation between the various error metrics can be attributed to the nonlinear interaction between the different ionic channels. Thus, the competing roles of sodium and potassium currents affects primarily the amplitude and spike width which shape the action potential.

To assess the variability across the different parameters for each neuron, we analyzed the parameter set corresponding to the minimum error. Figure 24-25 show the box plots corresponding to the values of  $k_{1x}$  through  $k_{13x}$ . The observed spread in the  $k$  parameters emphasizes intrinsic variability among neurons and indicates that neuron-specific parameter sets are necessary to accurately capture their electrophysiological behavior.

In our study, we use a feature–feature error metric graphs to visualize trade-offs between different electrophysiological features. These plots highlight that no single global minimum error solution can be attained, as different spike features impose different constraints. This highlights the presence of competing constraints in the model among the different features. As a result, it becomes essential to define which features are the most significant to the scientific question at hand. The trade-off graphs not only identify reasonable regions of parameter space that produce good model performance, but can also provide biological insight — for example, persistent conflicts between features may indicate that an additional ionic mechanism is required in the model. Ultimately, the

choice of optimization target depends on the modeling goal: in some contexts, accurately reproducing first-spike latency is critical, such as in models of early sensory processing, whereas in other studies overall firing rate or spike morphology may be the primary feature of interest (Druckmann, 2007). Consequently, the choice of the optimal parameter set depend on which aspect of the biological response that. This is important in neuronal models where each feature of the spike is biologically significant. Using a single combined error metric may give us a single value but may not reflect a true decent fit. Thus, optimization process should be tailored to specific modeling objectives as well as parameters.

## CHAPTER V

### CONCLUSION

In this study, we developed a feature – based optimization process to improve the fitting of the Hodgkin Huxley model to biological recordings. By modifying the channel kinetics and exploring large parameter space of the specific parameters related to the gating variables, we were able to reproduce spikes times and morphology across multiple HVC<sub>x</sub> neurons. We tackled the kinetics of the activating and inactivating gating variables through the specific parameters that directly influence shape of the action potential. Our results demonstrate that no single universal parameter can be used to simulate a neuronal model and capture the true dynamics of the model. This highlights the intrinsic variability among different neurons. Therefore, to model neurons effectively it is essential tailor parameters specifically for each system. Trade off analysis revealed competing constraints between spike features. This conclusion emphasizes that optimization objectives must be selected based on the physiological properties of interest. Finally, testing the models under pseudo noisy stimuli showed that tailored parameter sets generalize to complex input conditions, highlighting the importance of adjusting the model parameters specifically for each neuron as a necessity and not just as a technical step to build a realistic conductance based model.

## REFERENCES

- Abarbanel, H. D. I., Rozdeba, P. J., & Shirman, S. (2018). Machine Learning: Deepest Learning as Statistical Data Assimilation Problems. *Neural Computation*, 30(8), 2025-2055. [https://doi.org/10.1162/neco\\_a\\_01094](https://doi.org/10.1162/neco_a_01094)
- Amendola, M., Arcucci, R., Mottet, L., Casas, C. Q., Fan, S., Pain, C., Linden, P., & Guo, Y.-K. (2020). Data assimilation in the latent space of a neural network. *arXiv preprint arXiv:2012.12056*.
- Asari, H., & Zador, A. M. (2009). Long-lasting context dependence constrains neural encoding models in rodent auditory cortex. *J Neurophysiol*, 102(5), 2638-2656. <https://doi.org/10.1152/jn.00577.2009>
- Brette, R., & Gerstner, W. (2005). Adaptive Exponential Integrate-and-Fire Model as an Effective Description of Neuronal Activity. *J Neurophysiol*, 94(5), 3637-3642. <https://doi.org/10.1152/jn.00686.2005>
- Catterall, W. A., Raman, I. M., Robinson, H. P., Sejnowski, T. J., & Paulsen, O. (2012). The Hodgkin-Huxley heritage: from channels to circuits. *J Neurosci*, 32(41), 14064-14073. <https://doi.org/10.1523/jneurosci.3403-12.2012>
- Daou, A., & Margoliash, D. (2020). Intrinsic neuronal properties represent song and error in zebra finch vocal learning. *Nat Commun*, 11(1), 952. <https://doi.org/10.1038/s41467-020-14738-7>
- He, F., & Yang, Y. (2021). Nonlinear System Identification of Neural Systems from Neurophysiological Signals. *Neuroscience*, 458, 213-228. <https://doi.org/10.1016/j.neuroscience.2020.12.001>

- Hodgkin, A. L., & Huxley, A. F. (1952). A quantitative description of membrane current and its application to conduction and excitation in nerve. *J Physiol*, *117*(4), 500-544. <https://doi.org/10.1113/jphysiol.1952.sp004764>
- Houghton, C., & Victor, J. D. (2011). Measuring Representational Distances: The Spike-Train Metrics Approach. In N. Kriegeskorte & G. Kreiman (Eds.), *Visual Population Codes: Toward a Common Multivariate Framework for Cell Recording and Functional Imaging* (pp. 0). The MIT Press. <https://doi.org/10.7551/mitpress/8404.003.0012>
- Izhikevich, E. M. (2003). Simple model of spiking neurons. *IEEE Transactions on neural networks*, *14*(6), 1569-1572.
- Klausberger, T., & Somogyi, P. (2008). Neuronal diversity and temporal dynamics: the unity of hippocampal circuit operations. *Science*, *321*(5885), 53-57. <https://doi.org/10.1126/science.1149381>
- Kreuz, T., Chicharro, D., Houghton, C., Andrzejak, R. G., & Mormann, F. (2013). Monitoring spike train synchrony. *Journal of Neurophysiology*, *109*(5), 1457-1472. <https://doi.org/10.1152/jn.00873.2012>
- Kumar, G., Aggarwal, V., Thakor, N. v., Schieber, M., & Kothare, M. V. (2010). *Optimal parameter estimation of the Izhikevich single neuron model using experimental Inter-Spike Interval (ISI) data*. <https://doi.org/10.1109/ACC.2010.5530803>
- Li, Q., Calhoun, V. D., Pham, T. D., & Iraji, A. (2024). Exploring Nonlinear Dynamics In Brain Functionality Through Phase Portraits And Fuzzy Recurrence Plots. *bioRxiv*. <https://doi.org/10.1101/2023.07.06.547922>

- Liu, J., Tu, H., Zhang, D., Zheng, H., & Li, Y. L. (2012). Voltage-gated sodium channel expression and action potential generation in differentiated NG108-15 cells. *BMC Neurosci*, *13*, 129. <https://doi.org/10.1186/1471-2202-13-129>
- Louise Faber, E. (2009). Functions and modulation of neuronal SK channels. *Cell biochemistry and biophysics*, *55*, 127-139.
- Ludwig, A., Zong, X., Jeglitsch, M., Hofmann, F., & Biel, M. (1998). A family of hyperpolarization-activated mammalian cation channels. *Nature*, *393*(6685), 587-591. <https://doi.org/10.1038/31255>
- Milescu, L. S., Yamanishi, T., Ptak, K., & Smith, J. C. (2010). Kinetic properties and functional dynamics of sodium channels during repetitive spiking in a slow pacemaker neuron. *J Neurosci*, *30*(36), 12113-12127. <https://doi.org/10.1523/jneurosci.0445-10.2010>
- Miller, A., Li, D., Platt, J., Daou, A., Margoliash, D., & Abarbanel, H. D. I. (2018). Statistical Data Assimilation: Formulation and Examples From Neurobiology [Original Research]. *Frontiers in Applied Mathematics and Statistics*, *4*. <https://doi.org/10.3389/fams.2018.00053>
- Morris, C., & Lecar, H. (1981). Voltage oscillations in the barnacle giant muscle fiber. *Biophys J*, *35*(1), 193-213. [https://doi.org/10.1016/s0006-3495\(81\)84782-0](https://doi.org/10.1016/s0006-3495(81)84782-0)
- Ranjan, R., Khazen, G., Gambazzi, L., Ramaswamy, S., Hill, S. L., Schürmann, F., & Markram, H. (2011). Channelpedia: an integrative and interactive database for ion channels. *Front Neuroinform*, *5*, 36. <https://doi.org/10.3389/fninf.2011.00036>
- Satuvuori, E., & Kreuz, T. (2018). Which spike train distance is most suitable for distinguishing rate and temporal coding? *Journal of neuroscience methods*, *299*, 22-33.

- Schreiber, S., Fellous, J.-M., Whitmer, D., Tiesinga, P., & Sejnowski, T. J. (2003). A new correlation-based measure of spike timing reliability. *Neurocomputing*, 52, 925-931.
- Sherwood, W. E. (2013). FitzHugh–Nagumo Model. In D. Jaeger & R. Jung (Eds.), *Encyclopedia of Computational Neuroscience* (pp. 1-11). Springer New York.  
[https://doi.org/10.1007/978-1-4614-7320-6\\_147-1](https://doi.org/10.1007/978-1-4614-7320-6_147-1)
- Shettigar, N., Yang, C.-L., Tu, K.-C., & Suh, C. S. (2022). On The Biophysical Complexity of Brain Dynamics: An Outlook. *Dynamics*, 2(2), 114-148.  
<https://www.mdpi.com/2673-8716/2/2/6>
- Stafstrom, C. E. (2007). Persistent sodium current and its role in epilepsy. *Epilepsy Curr*, 7(1), 15-22. <https://doi.org/10.1111/j.1535-7511.2007.00156.x>
- Stiles, J., & Jernigan, T. L. (2010). The basics of brain development. *Neuropsychol Rev*, 20(4), 327-348. <https://doi.org/10.1007/s11065-010-9148-4>
- Tsuda, I. (2001). Toward an interpretation of dynamic neural activity in terms of chaotic dynamical systems. *Behavioral and Brain Sciences*, 24(5), 793-810.  
<https://doi.org/10.1017/S0140525X01000097>
- Van Rossum, M. C. (2001). A novel spike distance. *Neural Computation*, 13(4), 751-763.
- Victor, J. D., & Purpura, K. P. (1996). Nature and precision of temporal coding in visual cortex: a metric-space analysis. *J Neurophysiol*, 76(2), 1310-1326.
- Wilson HR, Cowan JD. Excitatory and inhibitory interactions in localized populations of model neurons. *Biophys J*. 1972 Jan;12(1):1-24. doi: 10.1016/S0006-3495(72)86068-5. PMID: 4332108; PMCID: PMC1484078.
- Zeng, Y., Bao, W., Tao, L., Hu, D., Yang, Z., Yang, L., & Shang, D. (2022). Regularized Spectral Spike Response Model: A Neuron Model for Robust Parameter

Reduction. *Brain Sciences*, 12(8), 1008. <https://www.mdpi.com/2076-3425/12/8/1008>